Article

Cell Reports

Chronic FLT3-ITD Signaling in Acute Myeloid Leukemia Is Connected to a Specific Chromatin Signature

Graphical Abstract

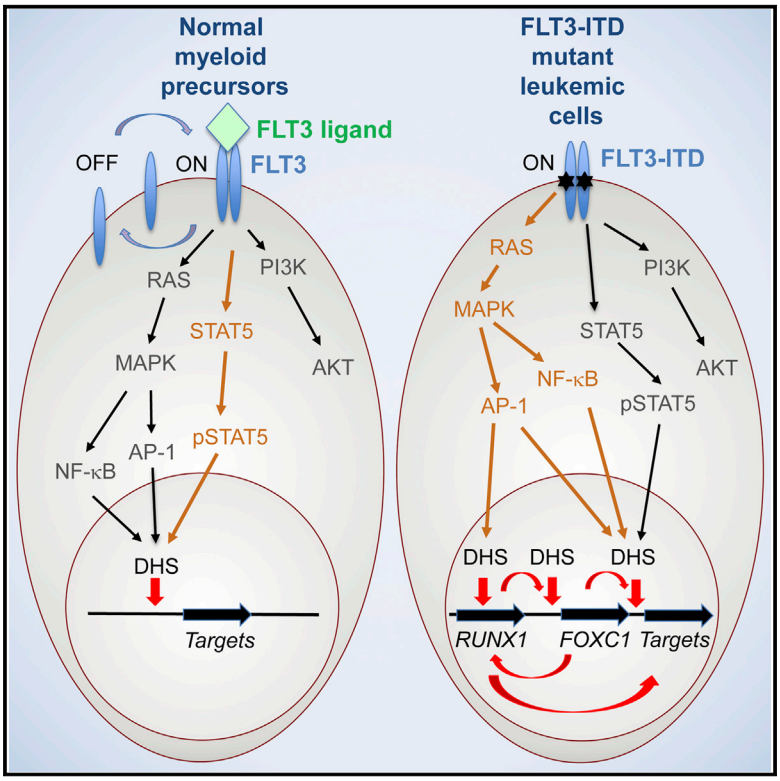

Authors

Pierre Cauchy, Sally R. James, Joaquin Zacarias-Cabeza, ..., Sascha Ott, Constanze Bonifer, Peter N. Cockerill

Correspondence

c.bonifer@bham.ac.uk (C.B.), p.n.cockerill@bham.ac.uk (P.N.C.)

In Brief

Cauchy et al. identify a specific gene expression and regulatory signature associated with aberrant signaling in acute myeloid leukemia with FLT3-ITD mutations. In FLT3-ITD AML, the inducible transcription factor AP-1 is chronically activated and cooperates with RUNX1, shaping the epigenome to transactivate specific target genes.

Highlights

- FLT3-ITD signaling is associated with a common gene expression signature
- FLT3-ITD-specific gene expression is associated with a common chromatin signature
- FLT3-ITD AML displays chronic activation of the inducible transcription factor AP-1
- AP-1 cooperates with RUNX1 to shape the epigenome of FLT3-ITD AML

Accession Numbers

GSE64874

Cauchy et al., 2015, Cell Reports *12*, 821–836
August 4, 2015
http://dx.doi.org/10.1016/j.celrep.2015.06.069

CellPress

Cell Reports
Article

Chronic FLT3-ITD Signaling in Acute Myeloid Leukemia Is Connected to a Specific Chromatin Signature

Pierre Cauchy,[1] Sally R. James,[2] Joaquin Zacarias-Cabeza,[1] Anetta Ptasinska,[1] Maria Rosaria Imperato,[1] Salam A. Assi,[2] Jason Piper,[3] Martina Canestraro,[1] Maarten Hoogenkamp,[1] Manoj Raghavan,[1,4] Justin Loke,[1] Susanna Akiki,[5] Samuel J. Clokie,[5] Stephen J. Richards,[6] David R. Westhead,[7] Michael J. Griffiths,[1,5] Sascha Ott,[3] Constanze Bonifer,[1,*] and Peter N. Cockerill[8,*]

[1]School of Cancer Sciences, College of Medicine and Dentistry, University of Birmingham, Birmingham B15 2TT, UK
[2]Section of Experimental Haematology, Leeds Institute for Molecular Medicine, University of Leeds, Leeds LS9 7TF, UK
[3]Warwick Systems Biology Centre, University of Warwick, Coventry CV4 7AL, UK
[4]Centre for Clinical Haematology, Queen Elizabeth Hospital, Birmingham B15 2TH, UK
[5]West Midlands Regional Genetics Laboratory, Birmingham Women's NHS Foundation Trust, Birmingham B15 2TG, UK
[6]Haematological Malignancy Diagnostic Service, St. James's University Hospital, Leeds LS9 7TF, UK
[7]School of Molecular and Cellular Biology, Faculty of Biological Sciences, University of Leeds, Leeds LS2 9JT, UK
[8]School of Immunity and Infection, College of Medicine and Dentistry, University of Birmingham, Birmingham B15 2TT, UK
*Correspondence: c.bonifer@bham.ac.uk (C.B.), p.n.cockerill@bham.ac.uk (P.N.C.)
http://dx.doi.org/10.1016/j.celrep.2015.06.069

SUMMARY

Acute myeloid leukemia (AML) is characterized by recurrent mutations that affect the epigenetic regulatory machinery and signaling molecules, leading to a block in hematopoietic differentiation. Constitutive signaling from mutated growth factor receptors is a major driver of leukemic growth, but how aberrant signaling affects the epigenome in AML is less understood. Furthermore, AML cells undergo extensive clonal evolution, and the mutations in signaling genes are often secondary events. To elucidate how chronic growth factor signaling alters the transcriptional network in AML, we performed a system-wide multi-omics study of primary cells from patients suffering from AML with internal tandem duplications in the FLT3 transmembrane domain (FLT3-ITD). This strategy revealed cooperation between the MAP kinase (MAPK) inducible transcription factor AP-1 and RUNX1 as a major driver of a common, FLT3-ITD-specific gene expression and chromatin signature, demonstrating a major impact of MAPK signaling pathways in shaping the epigenome of FLT3-ITD AML.

INTRODUCTION

In cancer, genes encoding signaling molecules and transcription factors (TFs) can become mutated, thereby leading to changes in homeostatic gene regulatory networks, and a block in the normal program of terminal differentiation. This is also true for acute myeloid leukemia (AML). AML is a heterogeneous disease that is caused by multiple mutations that affect normal blood cell development from hematopoietic stem cells (HSCs) and prime developing cells to become malignant. However, during the progression of the leukemic state, pre-leukemic and leukemic cells undergo clonal evolution creating heterogeneous cell populations with different functional properties. In recent years it has become clear that the majority of initial mutations occur in genes encoding transcriptional and epigenetic regulators (Corces-Zimmerman et al., 2014; Corces-Zimmerman and Majeti, 2014). A few studies have examined in a system-wide fashion how leukemic TFs reprogram chromatin and establish specific epigenetic signatures and gene expression programs (Prange et al., 2014). An example for this notion is the case of AML with t(8;21) chromosomal translocation, which gives rise to the fusion protein RUNX1/ETO. This aberrant TF competes with RUNX1 for its binding motifs, leading to epigenetic reprogramming with a block in myeloid differentiation and the concomitant activation of a precursor-like AML-specific transcriptional network (Martens et al., 2012; Ptasinska et al., 2012, 2014). However, in the case of karyotypically normal (KN) AML, it has proved to be much harder to identify consistent patterns of deregulation associated with specific mutations. This difficulty is due to (1) the heterogeneous nature of the combinations of underlying mutations and (2) the fact that AML cells often span a range of differentiation states. There is the added complexity that mutations in genes encoding signaling molecules tend to appear late in the process of leukemogenesis, making it harder to definitively link them to consistent target gene alteration (Corces-Zimmerman et al., 2014). Some of the most frequent secondary mutations found in AML are in tyrosine kinase receptors such as FLT3 and KIT, which are rendered constitutively active (Masson and Rönnstrand, 2009). These receptors normally control the regulated growth and survival of myeloid progenitor cells. Mutations deregulate this process, thus effectively cutting off cancer cells

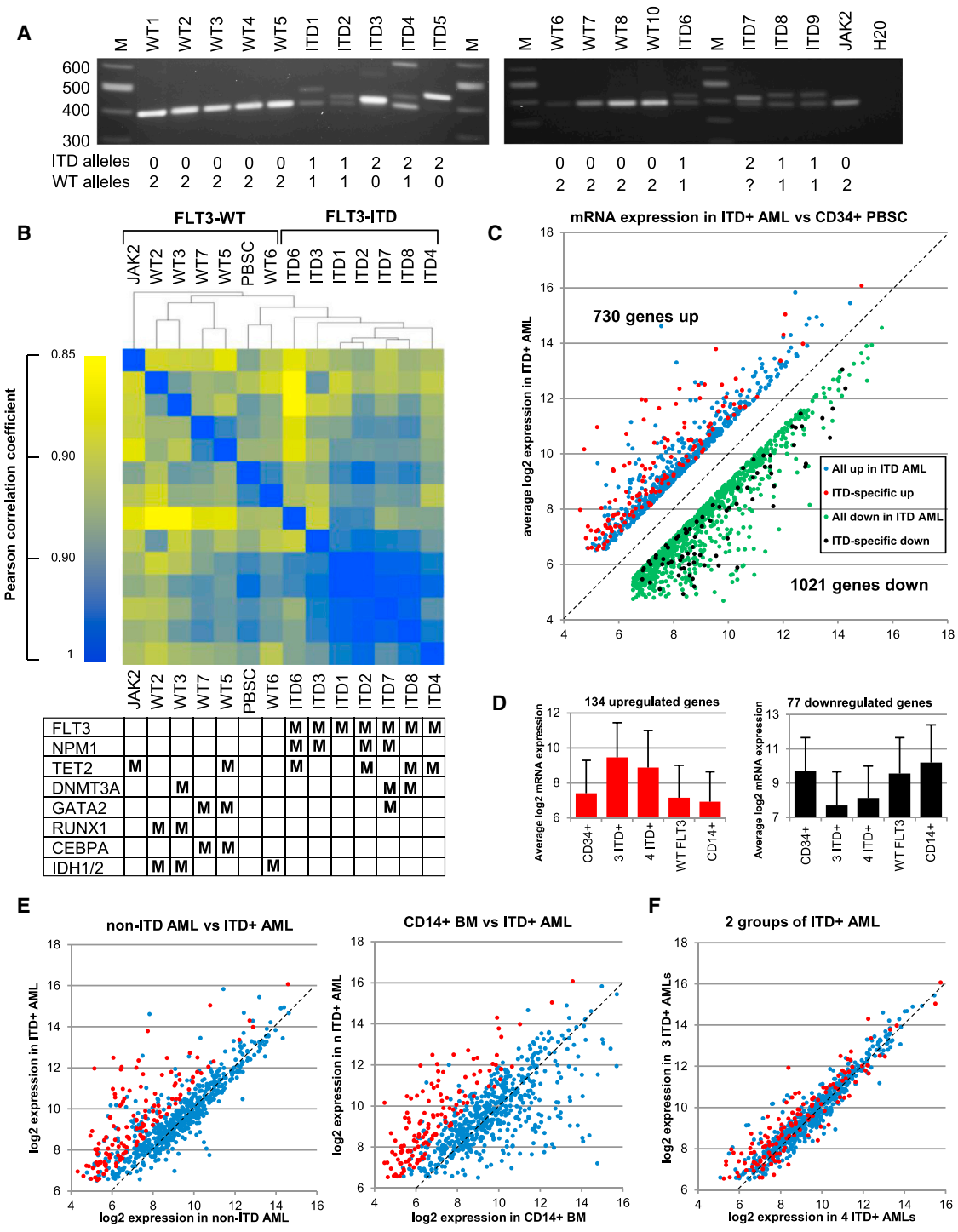

Figure 1. FLT3-ITD+ AML Displays a Characteristic mRNA Expression Profile

(A) PCR amplification of the transmembrane coding region of the FLT3 gene used to identify ITD mutations. On the left are the sizes of the DNA marker bands (M). Below are the estimated numbers of normal and mutated FLT3 alleles.

(B) Hierarchical clustering of Pearson correlation coefficients of mRNA values. For each sample the mutations present in the most commonly mutated genes are indicated as M in the table underneath.

(C–F) Identification of genes that differ by at least 2-fold in a comparison of the average log2 mRNA microarray values for a core group of three ITD+ AML samples (ITD1, ITD2, and ITD3) to the equivalent values determined from either the average of two independent PBSC samples (C), the average of four WT FLT3 AML samples (WT2, WT3, WT5, and WT7), for CD14+ bone marrow cells (E), or a second group of ITD+ AML samples (ITD4, ITD6, ITD7, and ITD8) used here for

(legend continued on next page)

from normal growth regulating controls. However, we currently know very little about how mutations in signaling molecule genes impact on gene expression and whether they also establish a common epigenetic signature.

To address this question, we focused on the identification of changes in the chromatin landscape and patterns of gene expression that are driven by constitutive activation of intracellular signaling pathways and concentrated on KN-AML with internal tandem duplications (ITDs) in the FLT3 transmembrane domain as a paradigm. FLT3-ITD mutations are found in ~25% of KN-AML and lead to constitutive activation of the downstream mitogen-activated protein kinase (MAPK), AKT, and signal transducer and activator of transcription (STAT) signaling pathways linked to FLT3 (Stirewalt and Radich, 2003; Thiede et al., 2002). FLT3-ITD frequently acts as a partner in AML with other mutations such as those in transcription factors, epigenetic regulators, and Nucleophosmin (NPM1). Tyrosine kinase receptor signaling has a direct influence on multiple signaling pathways (Gu et al., 2011; Scholl et al., 2008) and the activities of many TFs (Goyama et al., 2014; Yordy and Muise-Helmericks, 2000), but could also signal to chromatin directly (Badeaux and Shi, 2013; Dawson et al., 2009; Ray et al., 2013). Our goal was therefore to examine whether the presence of the FLT3-ITD leads to the establishment of a common epigenetic signature. To this end we mapped open regions of chromatin that exist as DNase I hypersensitive sites (DHSs) as this identifies active regulatory elements (Cockerill, 2011). Using complementary genome-wide analyses of gene expression and regulation in primary AML cells, we show that the FLT3-ITD mutation is associated with extensive changes in the epigenetic landscape and report a FLT3-ITD-specific gene expression signature that is associated with FLT3-ITD-specific DHSs. The integration of these global data reveals a cooperation between the MAPK inducible transcription factor AP-1 and RUNX1 as two of the main drivers of a FLT3-ITD-specific open chromatin signature.

RESULTS

System-wide Genomic and Epigenomic Analysis of Karyotypically Normal AML

In order to define the specific genomic targets of aberrant signaling in KN AML with the FLT3-ITD mutation, we purified undifferentiated CD34 or CD117 positive cells, or obtained a mononuclear fraction comprising greater than 92% undifferentiated blast cells, either from peripheral blood or from bone marrow of AML patients. This protocol avoided confounding issues associated with contamination by differentiated cells expressing markers unrelated to leukemogenesis. Profiles from AML cells were compared to those of the CD34+ progenitor population of mobilized peripheral blood stem cells (PBSCs). To identify specific genetic and epigenetic signatures, we performed a comprehensive set of genome-wide analyses that included (1) global mRNA microarray analysis to identify aberrantly regulated genes, (2) a DNA sequence screen for exonic mutations within 55 candidate myeloid oncogenes and tumor suppressor genes to uncover pathways responsible for aberrant gene expression patterns (Table S1), (3) global DNase sequencing (DNase-seq) mapping of DHS patterns to identify aberrantly activated (and absent) *cis*-regulatory elements, (4) identification of regions within DHSs protected from DNase I digestion (digital footprints), and the underlying specific motifs bound by TFs, (5) chromatin immunoprecipitation sequencing (ChIP-seq) assays to detect specific proteins bound at DHSs, and (6) DNA methylation array analysis of 450,000 CG sites to detect epigenetically silenced loci. These analyses included 19 KN AML samples, of which 9 were from FLT3-ITD+ patients. Because the exon sequencing screen was unable to detect all of the FLT3-ITD mutations, which vary greatly in size and location, we confirmed the predicted FLT3-ITD status by PCR analyses (Figure 1A), which indicated that the ITD had occurred on both alleles in three of the samples (ITD3, ITD5, and ITD7), while ITD4 had two different forms of the ITD mutation. Data File S1 describes all of the mutations in all our samples, which were found in 21 different genes, plus their allele frequencies. Most of these mutations and FLT3 PCR products were detected at levels close to 50% or 100%, indicating that these samples were clonal and that some mutations such as those in *JAK2* were bi-allelic. Of the nine ITD+ patients, one sample had no other defined mutations (ITD1), and this became the prototype ITD+ sample anchoring this study. Three of the patients with wild-type (WT) FLT3 had mutations in genes encoding other signaling molecules linked to FLT3 signaling pathways, which included *NRAS*, *PTN11*, *SOCS1*, and *JAK2*, which might therefore share some common features with FLT3-ITD+ AML. *SOCS1* mutations are also known to cooperate with FLT3-ITD in AML (Reddy et al., 2012).

AML with FLT3-ITD Displays a Specific Gene Expression Profile

We used microarray analysis to define mRNA levels for ~22,000 genes for AML samples and in 2 independent samples of CD34+ PBSCs. Hierarchical clustering of the Pearson correlation coefficients was then used to identify similarities and differences between these AMLs (Figure 1B). This analysis included seven FLT3-ITD+ AMLs, five AMLs with wild-type (WT) FLT3 (and no other known receptor mutations), and one AML with an activating JAK2 mutation (and WT FLT3). The seven ITD+ AMLs formed a discrete cluster with high correlation coefficients, while the five WT FLT3 AMLs clustered more closely with the PBSCs, and the JAK2 mutated AML had a pattern distinctly different to all the other samples. The parallel mutation analysis revealed that mutations in the epigenetic regulators DNMT3A and TET2 were divided between the FLT3-ITD+ and WT FLT3 groups, and mutations in the genes encoding the TFs RUNX1, GATA2, and C/EBPα occurred predominantly in the WT FLT3 AMLs. NPM1 mutations,

validation of the ITD+ pattern (F). The 134 genes that are consistently expressed at 2-fold higher levels in ITD+ AML in each of the three comparisons in (C) and (E) are shown in red, and the remaining genes that are upregulated in at least (C) are shown in blue. In (C) we also highlight 77 genes with values that are consistently 2-fold lower in ITD+ AML compared to each of PBSCs, WT FLT3 AML, and CD14+ cells in black, and the remaining genes that are also downregulated at least in (B) are shown in green. (D) Average log2 mRNA values for the specific groups of 134 upregulated and 77 downregulated genes in each of the 5 groups used in this analysis, with the SD for mRNA expression shown as error bars.

which frequently partner FLT3-ITD, were restricted to the FLT3-ITD+ AML cluster, but could not alone account for the observed patterns as they did not independently cluster together.

To identify a set of genes specifically deregulated in FLT3-ITD+ AML, we focused on the most related samples from each group and independently analyzed expression data from three core ITD+ AMLs (ITD1, ITD2, and ITD3) and four core WT FLT3 AMLs (WT2, WT3, WT5, and WT7), for which we also had accompanying DHS data. The three ITD+ AMLs included two with mutated NPM1 (ITD2 and ITD3) plus ITD1 with no other defined mutations (Data File S1). We compared the average log2 mRNA microarray values with those for CD34+ PBSCs. As an additional control and to assess the stage of the differentiation block, we also compared these values with those from normal bone-marrow derived CD14+ myeloid cells. We used this second criterion to assist in the identification of artifacts arising from high levels of gene expression within minor subsets of more differentiated monocytic cells.

Within the core group of 3 ITD+ AMLs, we identified 730 upregulated genes with average log2 values at least 1.0 above PBSCs, (and absolute log2 values of at least 6.5 to select genes at least 1 log above background), plus 1,021 downregulated genes with values at least 1.0 below that of PBSCs (blue and green dots, Figure 1C). However, only 134 of the upregulated genes and 77 of the downregulated genes maintained the same specific pattern of deregulation relative to both the WT FLT3 AML subset and the CD14+ve cells (Figures 1C–1E, represented by red and black dots). Note that some of the 730 genes upregulated in ITD+ cells were expressed at very high levels in CD14+ cells, meaning that the elevated values may have arisen from a minor contamination with more differentiated cells. The 134 ITD-specific genes were on average expressed at levels 4-fold higher than in PBSCs, WT FLT3 AML, and CD14+ve cells (Figure 1D). Conversely, the 77 downregulated genes were on average expressed at levels 4-fold lower than the other three cell types. We confirmed the generality of these observations by demonstrating that the gene expression profile for the genes upregulated in the core ITD+ group was essentially identical to the average mRNA profile observed for an additional group of four other ITD+ AMLs (ITD4, ITD6, ITD7, and ITD8) (Figure 1F). These analyses highlighted the need for more than one reference cell type when assessing expression patterns to identify true FLT3-ITD responsive genes. Our data also suggest that the block in differentiation in the FLT3-ITD+ AML occurs further down the myeloid differentiation pathway as indicated by the presence of the many genes expressed at levels similar to those in more mature CD14+ve cells (and the WT FLT3 AML), but higher than in PBSCs.

The average values for mRNA expression for the above two groups of deregulated genes are listed in Data File S2. They include upregulated genes that could influence the development of AML cells such as genes encoding (1) the transcriptional regulators *FOXC1*, *PRDM16* (MEL1), and *NFIX*, (2) growth factor receptor genes such as *IL2RA*, *IL3RA*, *TNFSF9*, *TNFRSF4*, and *TNFRSF18*, (3) additional genes influencing growth and survival such as *CCNA1* (Cyclin A), *PTP4A3* (PRL3), and *IGFBP2*, (4) genes controlling differentiation such as the *HOXB2* to *HOXB6* cluster, and *PBX3*, (5) genes controlling homing such as the chemokine genes *CCL1* and *CCL5*, and (6) genes for proteases that are known to remodel tissues and enhance migration such as *CTSG*, *ADAMTS14*, *MMP15*, and (7) a gene cluster that includes the protease genes *ELANE*, *PRTN3*, and *AZU1* as well as *LPPR3*. The upregulated class of genes also contained other potentially important genes regulating signaling and migration such as *AK2* (adenylate cyclase), *DSC2* (a protein involved in cell adhesion), and the gene encoding the macrophage scavenger receptor *SCARA3*, which may be related to the fact that FLT3-ITD cells increase ROS production (Sallmyr et al., 2008). *FOXC1* encodes a pioneer-type transcription factor (Zaret and Carroll, 2011). PRDM16 is related to the cancer-promoting histone methyl transferase gene *EVI1*, and both *EVI1* and *PRDM16* are activated via RAS mutations in models of myeloid leukemia (Wolf et al., 2013).

The expression patterns of seven of these upregulated genes, plus TBP as a control, are shown in Figure S1A for all of the samples analyzed. Within the core cluster of three ITD+ AMLs, *FOXC1* was the only FOX gene significantly upregulated in ITD+ AML compared to the cluster of four WT FLT3 AMLs, while *FOXO1* expression was downregulated (Figure S1B). Most notable of the 77 downregulated genes was a group of 10 HLA class II genes that were consistently downregulated in ITD+ AML and not in WT FLT3 AML (Figure S1C).

To validate the conclusions of our mRNA expression analysis, we analyzed data from two published studies of much larger cohorts of AML samples (Figure 2). For the ITD target genes identified above, we calculated the average mRNA levels for data from (1) a study of 461 AML patients comparing FLT3 ITD+AML samples with WT FLT3 AML samples (Verhaak et al., 2009) and (2) a study of 200 patients from The Cancer Genome Atlas (TCGA) Research Network comparing all samples with any FLT3 mutations with WT FLT3 AML samples (Cancer Genome Atlas Research Network, 2013). This confirmed that on average the above 134 upregulated genes and 77 downregulated genes displayed the same behavior in these much larger studies (Figures 2A and 2B). Several genes controlling gene expression or cell growth were confirmed as upregulated ITD target genes (Figure 2A), including *RUNX1*, *IGFBP2*, *PRDM16*, *PTP4A3*, and *CCNA1* (Figure 2C).

AML with FLT3-ITD Displays a Distinct Chromatin Signature

Tumor-specific DHSs patterns provide vital clues regarding the nature of TFs involved in tumorigenesis (Kreher et al., 2014). To identify DHSs specifically enriched in the ITD+ AMLs, we performed DNase-seq on a matched set of five ITD+ AMLs, five AMLs with WT FLT3, and two independent samples of CD34+ PBSCs. In a global evaluation of all the DHSs detected, we first identified all peaks for each dataset and determined the sequence tag counts for 400-bp regions centered on each peak. We then divided the peaks into the two separate groups of distal DHSs and promoter associated DHSs. Because we found that the greatest differences between the ITD+ and WT FLT3 AMLs were seen for the distal DHSs, we focused most of our subsequent more detailed analyses on this group. Previous global studies of transcriptional networks have similarly found that tissue-specific patterns are more associated with distal rather than proximal cis-elements (Heinz et al., 2010). For the

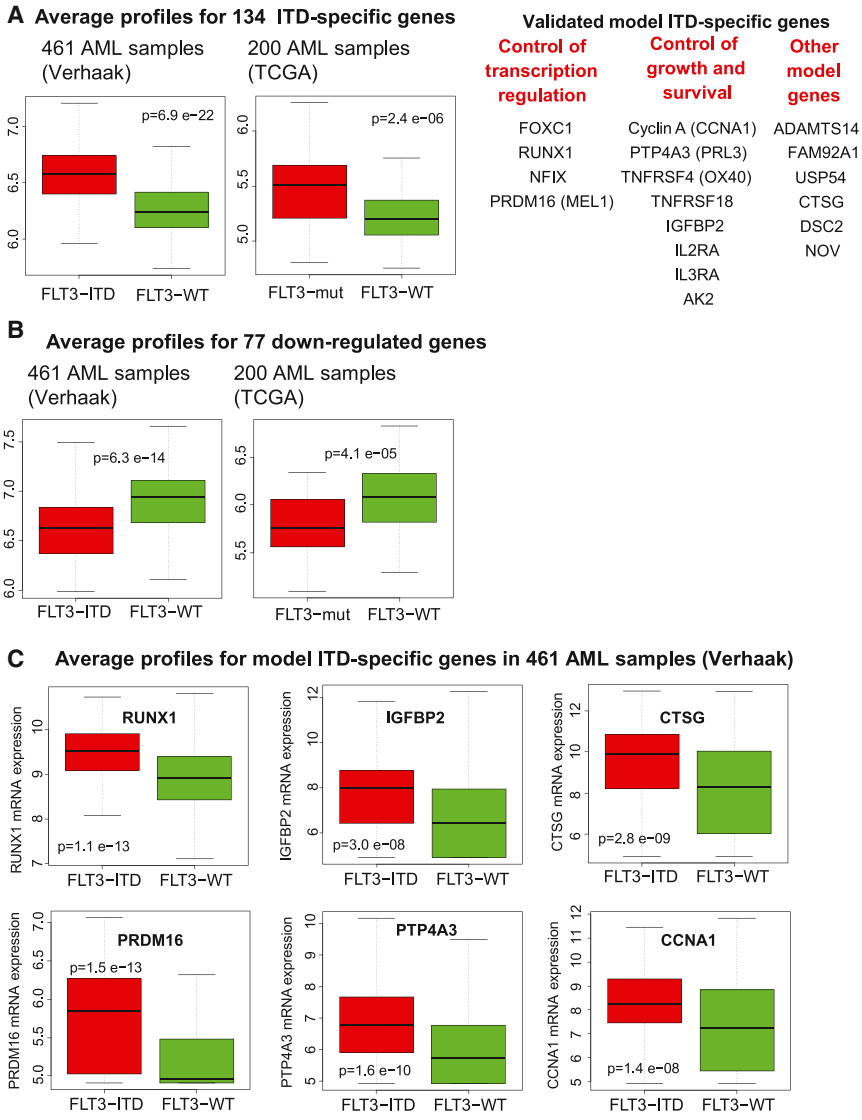

Figure 2. FLT3-ITD Consistently Deregulates the Same Genes in AML

(A–C) Average mRNA microarray values for FLT3-ITD target genes in 2 datasets obtained from 461 (Verhaak et al., 2009) or 200 (Cancer Genome Atlas Research Network, 2013) AML samples.

(A) Average profiles for 134 upregulated genes, with a subset of validated genes listed on the right.

(B) Average profiles for 77 downregulated genes.

(C) Profiles for individual upregulated genes.

initial comparisons, we performed hierarchical correlation clustering of the DNase-seq peak data (Figure 3A). As seen for the mRNA microarray values, the ITD+ samples clustered together as a discrete group distinct from both the WT FLT AMLs and the PBSCs. Parallel analysis of mutations in these samples again suggested that the ITD mutation had the greatest influence in defining the overall patterns of distal DHSs (Figure 3A, bottom). Interestingly, within the WT FLT3 group the two AMLs with mutated *RUNX1* genes clustered together, as did the two samples with both *GATA2* and *CEBPA* mutations.

Figure 3B depicts the genome browser view of a gene cluster that includes the myeloid genes *LPPR3*, *AZU1*, *PRTN3*, *ELANE*, and *CFD*. Four of these closely linked genes were included in the group of 134 highly ITD-specific mRNAs listed in Data File S2. This region includes an ITD-specific DHS within an intron of *MED16*, which was essentially absent in both CD34+ PBSCs and in AMLs with WT FLT3. Figure 3C reveals a strong trend for specific upregulation of expression of the whole cluster of five genes in the ITD+ samples (shown in red), with a modest upregulation of *MED16*, which harbors the specific DHS, and no upregulation of the flanking genes. With the exception of AML sample WT1, which carries a NRAS mutation, these upregulated genes were actually downregulated in AML with WT FLT3 (shown in green).

To visualize the overall specific DHS pattern in FLT3-ITD AML, we calculated the ratios for all of the distal DNase-seq peaks for each of the AML samples depicted in Figure 3A relative to the same regions, using a PBSC DNase-seq dataset that was sequenced at high read depth. These ratios were then used for hierarchical clustering of the values, which are represented as a heatmap in Figure 3D. This analysis identified a cluster of ~2,000 DHSs that were consistently enriched in the ITD+ samples and under-enriched in the WT FLT3 samples. Conversely, a separate cluster of DHSs was consistently downregulated in ITD+ AML and upregulated in the WT FLT3 samples, indicating that FLT3-ITD has both positive and negative effects on DHSs.

We next identified the full complement of FLT3-ITD-specific DHS peaks by calculating ratios of DNase-seq tag counts for all distal peaks detected in each AML sample and/or the PBSCs. Peaks were ranked in order of increasing DNase-seq tag count ratios for the AML sample relative to CD34+ PBSCs, and the DNase-seq data were plotted in order of increasing ratio as density maps spanning each 400-bp window. In the case of the prototype ITD+ AML sample ITD1 (which had no other defined mutations), we identified a total of 19,551 distal peaks present either in the ITD1 or PBSC dataset. The DNase-seq density maps are shown side-by-side in Figure 3E for both PBSCs and ITD1, revealing that most DHSs spanned ~200–250 bp and identifying a group of 3,728 distal DHSs that were at least 2-fold more intense in ITD1 (boxed region in Figure 3E). Parallel pair-wise analyses were also performed comparing the distal peaks in ITD2 and in ITD3, and the promoter-associated DHSs in ITD1, ITD2, and ITD3, with the equivalent regions in PBSCs (Figures S2A–S2C). In each case we identified the subsets of DHSs that

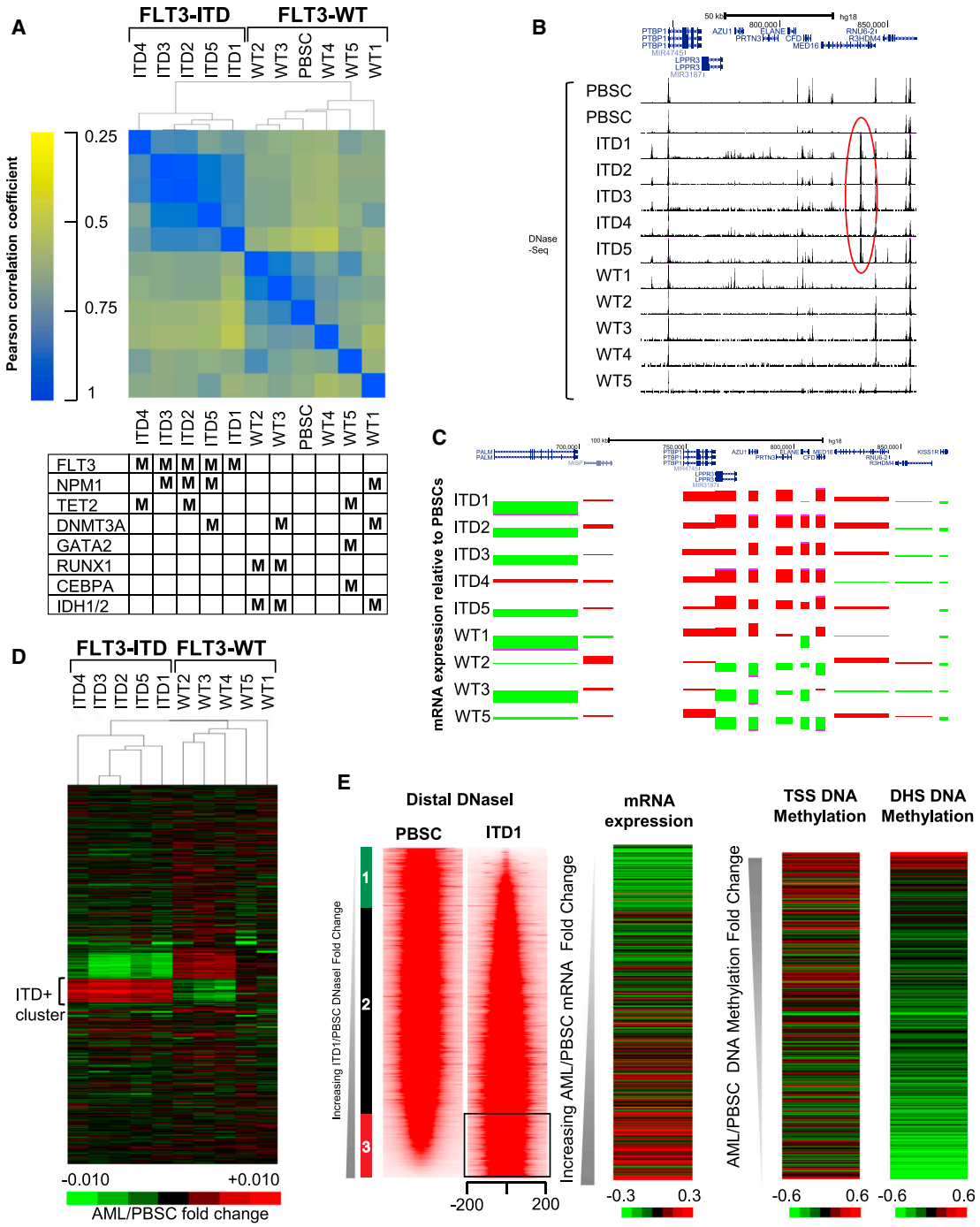

Figure 3. FLT3-ITD+ AML Has a Characteristic Chromatin Signature

(A) Hierarchical clustering of Pearson correlation coefficients of DHS peaks. For each sample the mutations present in the most commonly mutated genes are indicated as M in the table underneath.

(B and C) UCSC Genome Browser views of the DNase-seq patterns (B), and relative mRNA values (C) of genes surrounding an ITD+ AML-specific DHS in *MED16* marked by a red oval, and a cluster of adjacent genes upregulated in ITD+ AML. mRNA values are shown as a ratio of the values detected in the AML samples compared to PBSCs (red: up, green: down).

(D) Heatmap depicting hierarchical clustering of the relative DNase-seq signals seen in each distal DHS peak in each AML sample relative to PBSCs.

(E) Profiles of the DNase-seq signals within each 400-bp window centered on each peak for PBSC and ITD1, with peaks shown in the order of increasing DNase-seq tag count signal for ITD1 relative to PBSC. This analysis includes the union of all peaks present in either ITD1 or in PBSC. Shown to the right of the DNase-seq profiles are the relative mRNA expression values for genes with the nearest transcription start sites (TSS) in ITD1 relative to PBSC, and the DNA methylation signals for the nearest TSS and for the DHS in ITD1 relative to PBSCs.

were at least 2-fold more intense in the AML sample than in PBSCs. The profiles of the average tag counts for the distal DHSs are plotted in Figure S2D and reveal similar patterns of deregulation in each of ITD1, ITD2, and ITD3. The parallel analyses of the promoter regions showed a less pronounced upregulation of a small subset proximal DHSs in each of the ITD+ AML samples (Figure S2C).

To examine how the presence of DHSs impacted on the expression of nearby genes, we plotted the relative AML/PBSC mRNA expression levels for the genes nearest to each DHS in the three core FLT3-ITD AML samples relative to PBSCs (Figures 3E, S2A, and S2B). These heatmaps revealed a trend for upregulation of the genes nearest to ITD-specific DHSs. In parallel, we determined ratios for the level of DNA methylation for CG elements covered by the Illumina 450K platform, and we plotted heatmaps of this data for regions spanning both the DHS site itself and the transcription start site of the nearest gene for ITD1 and ITD2. This revealed a trend for DNA demethylation of both the ITD-specific DHSs and the adjacent transcription start sites (TSSs) and for increased DNA methylation in the DHSs that were absent (Figures 2E and S2A). However, the overall changes in DNA methylation were less pronounced than the chromatin changes, suggesting that these may be secondary events.

Using the ranking defined in Figure 3E, we also carried out direct side-by-side comparisons of the complete set of 19,551 distal ITD1/PBSC DHSs with each of the above datasets, plus the data for CD14+ BM cells, and for 3 previously published DHS datasets derived from normal CD34+ and CD14+ cells from the NIH Epigenome Roadmap consortium (Bernstein et al., 2010) plotted in the same order (Figure S2E). This confirmed that (1) the DHS pattern for PBSCs resembled independently derived equivalent CD34+ cell datasets, and (2) a common subset of DHSs was upregulated in each of the ITD+ samples, and (3) the DHS patterns present in the two more mature CD14+ cell datasets and the WT FLT3 AML samples more closely resembled PBSCs than ITD+ AML (Figure S2E). To better define these profiles, we used the relative DNase I signals to divide the DHSs into the three groups of (1) 2-fold downregulated, (2) less than 2-fold change, and (3) 2-fold upregulated (as depicted to the left of Figures 3E and S2E). The average DNase I profiles for each group are shown in Figure S2F. This clearly demonstrates that other ITD+ AMLs shared the same core of upregulated DHSs (group 3), whereas the patterns for the WT FLT AMLs more closely resembled the patterns for CD34+ and CD14+ cells. Last, but not least, we defined a discrete subset of reproducibly upregulated ITD-specific DHSs by determining the overlap between the FLT3-ITD-specific DHSs of each of ITD1, ITD2, and ITD3, and we found that 1,216 of these DHSs were shared between each group with high significance (Figure 4A). The locations of these DHSs are defined in Data File S3. ITD2 and ITD3, which both have NPM1 mutations, were the most similar with 83% of the top ITD2 group being part of the top ITD3 group. However, the NPM1 mutation is unlikely to be a major driver of this pattern because the upregulated DHSs from AML sample WT1 (Figure 4B) and WT8 (data not shown), which each carry an NPM1 mutation but WT FLT3, showed non-significant overlap with the ITD+ group. An equivalent analysis of the DHSs that are 2-fold upregulated in 3 AML samples with WT FLT3 (WT2, WT3, and WT5) also showed non-significant overlap with each other and with just 29 of the164 overlapping DHSs shared with the 1,216 ITD-specific DHSs (Figure 4C).

ITD-Specific DHSs Are Associated with ITD-Specific Genes and an Activation Signature

Gene ontology analysis of the genes located closest to the 1,216 distal ITD-specific DHSs identified a strong correlation with genes linked to cell signaling and activation (Figure 4D). To directly link the ITD-specific epigenetic signature with the gene expression profile, we calculated the distance of each ITD-specific gene promoter region from the nearest upregulated DHS for both the highly ITD-specific 134 genes (shown in red) and for the additional genes included in the 730 upregulated genes (shown in blue), and we depicted this relationship graphically in Figure 4E. Interestingly, this revealed an increasing degree of upregulation at the mRNA level for the genes closest to an ITD-specific DHS. Examples of individual ITD-specific genes close to ITD-specific DHSs are shown for *SCARA3*, *WDR86*, and *CTSG*/*GZMB* in Figures 4F and 4G and for *FOXC1*, *DSC2*, and *AK2* in Figures S1, S3A, and S3B. More complex patterns were seen for the *HOXB* cluster, where many DHSs were upregulated in ITD+ AML (Figure S3A), in parallel with the cluster of *HOXB2* to *HOXB6*, and for a DHS in the *C10orf128* locus, where both *C10orf128* locus and *VSTM4* were included in the group of 134 ITD-specific mRNAs (Figure S3B). A different pattern was seen for *ID1*, a previously defined ITD target gene (Tam et al., 2008), which contains an ITD-specific DHS at –2 kb and was upregulated in ITD+ AML compared to most WT FLT3 AMLs, but not compared to PBSC or normal CD14+ cells (Figure S3B). Interestingly, *ID1* is also regulated by a downstream STAT5-dependent enhancer at +5 kb (Tam et al., 2008; Wood et al., 2009). STAT5 is FLT3-ITD inducible (Mizuki et al., 2000). To examine the role of STAT5 in the regulation of this and other genes, we therefore measured genome-wide binding sites for this factor by ChIP-seq. This experiment demonstrates that the +5 kb element indeed binds STAT5 in the MV4-11 FLT3-ITD cell line (Figure S3B). However, this DHS was not FLT3-ITD-specific.

Overall, the ITD-specific genes were upregulated in either all or most ITD+ samples (Figures 4F and S1A). However, ITD9 represented a notable exception to this pattern. Interestingly, this patient carried a RUNX1 frameshift mutation, suggesting an important role of RUNX1 in activating FLT3-ITD-specific genes. Furthermore, the three samples carrying RUNX1 mutations (labeled R) tended to have similar expression profiles (WT2, ITD9, and WT3 in Figures 4, S1, and S3). Conversely, we also noted that among these loci there were also numerous examples of DHSs that were preferentially enhanced in both the ITD+ AMLs and in AML samples WT1 and/or WT6, which carry mutations in signaling molecules (labeled with asterisks). AML sample WT1 carries an activating NRAS G12S mutation, which is a powerful activator of the MAPK pathway. Hence, activating RAS mutations with a concomitant upregulation of MAPK signaling may activate a subset of genes and DHSs that we defined here as FLT3-ITD targets.

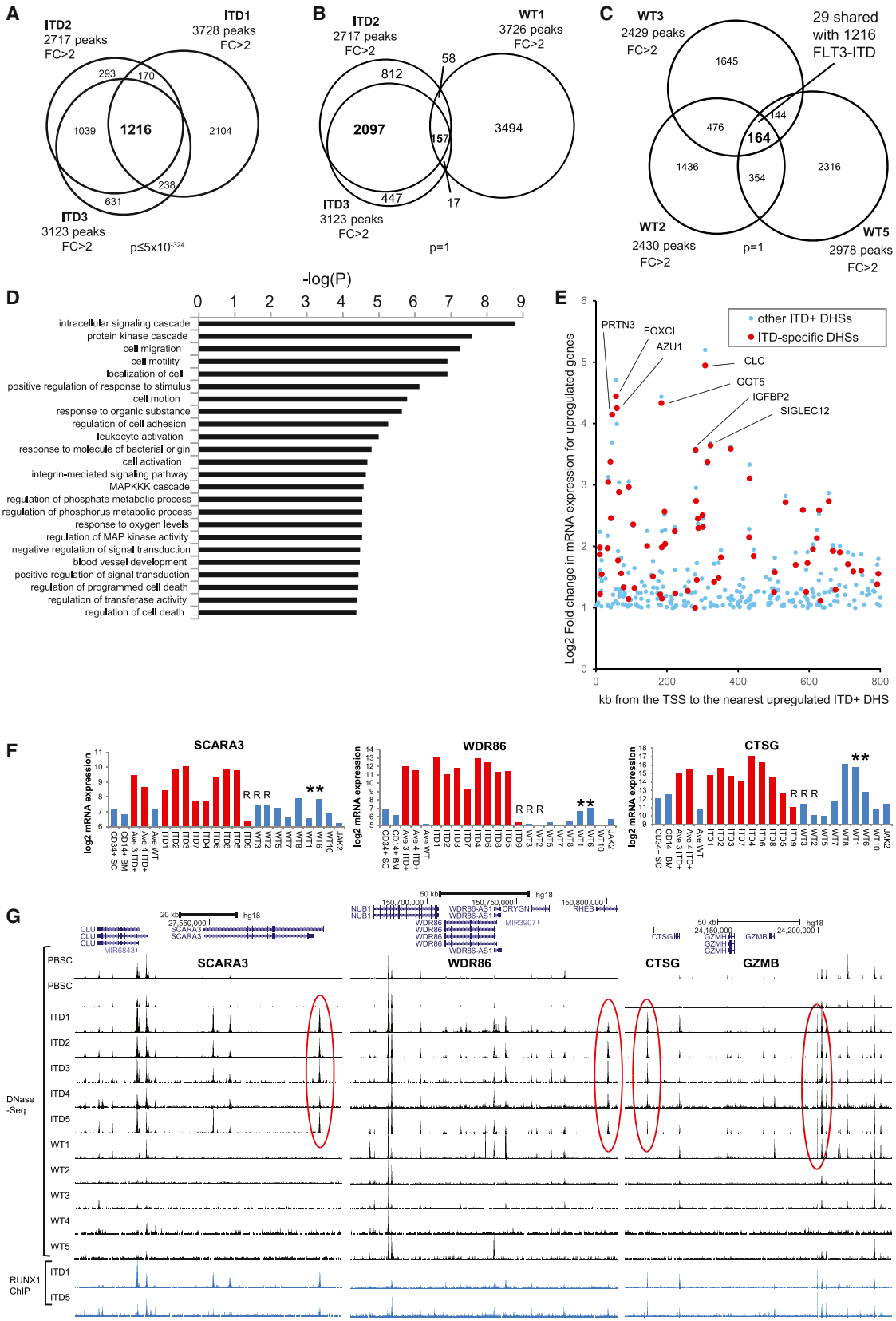

(legend on next page)

Taken together, our analysis demonstrates that in spite of the presence of a wide variety of mutations, the presence of a chronically active FLT3-ITD correlates with a common core epigenetic signature that is associated with a distinct gene expression pattern. In addition, our mutation data suggested a role for both RUNX1 and MAPK signaling in activating FLT3-ITD-specific DHSs.

FLT3-ITD-Specific DHSs Are Associated with Specific DNA Binding Motifs for RUNX1 and AP-1, but Not STAT5

Having identified a FLT3-ITD+ AML-specific epigenetic signature, we investigated its underlying molecular basis by performing an unbiased search for enriched sequence motifs within active chromatin regions using HOMER (Heinz et al., 2010) (Figure 5A). This analysis revealed that RUNX, AP-1, ETS, E-box, and C/EBP motifs were the most common binding motifs present in the top 1,216 ITD-specific DHSs, each being found in 18%–55% of all sites. Interestingly, we also identified a motif for Forkhead (FOX) family proteins, which was part of a composite FOX/E-box motif that might recruit complexes containing both FOX and HLH family TFs such as TAL1/SCL and LYL1, which function together with RUNX, ETS, and GATA family TFs in the combinatorial regulation blood stem cell development (Wilson et al., 2010). We also saw an enrichment of motifs for the inducible TFs NF-κB and ATF, but with less statistical significance. In order to validate the above results, we plotted the coordinates of each motif found back on to the coordinates of the DHSs, plotted in the same order of increasing DHS ratio as above (Figure 5B). We also plotted the rolling average of the numbers of each motif found per DHS across the same series of DHSs (Figure 5C), plus the average distributions of the motifs with each of the previously defined three groups of distal ITD1/PBSC DHSs (Figure S4A). All five motifs were present in the ITD-specific DHSs at levels substantially higher than the predicted random level (indicated by the dashed lines in Figure 5C). Most of these motifs aligned with the midpoints of the DHSs, suggesting that the two features are functionally related. Both the FOX/E-box and the C/EBP motifs were preferentially enriched in the ITD-specific DHSs, represented as group 3 in Figure S4A. ITD-specific DHSs were also highly enriched in motifs widely used in normal myeloid cells (Heinz et al., 2013). RUNX, ETS, and AP-1 motifs were highly abundant in both the ITD-specific DHSs and the DHSs that were shared between the AML and the PBSCs. This suggests that the FLT3-ITD signature involves a substantial degree of redeployment of TFs driving the normal myeloid program.

We also looked directly for the presence of binding motifs of other TFs linked to common signaling pathways that were not among the motifs found by HOMER, such as the FLT3-ITD inducible TF STAT5 (Mizuki et al., 2000). However, we did not see any significant enrichment for STAT motifs in ITD-specific DHSs or for motifs linked to other signaling pathways, such as interferon response factors (IRFs), which are common mediators of receptor signaling, or NFAT, which is a mediator of Ca^{2+} signaling (Figures S4A and S4B). These three classes of motifs were present at low abundance and mostly showed an anti-correlation with the ITD-specific DHSs. The average densities of each motif across each the three groups of DHS are depicted in Figure S4A. Because the TF GATA2 is important for blood stem cell development (de Pater et al., 2013; Wilson et al., 2010), we also analyzed the distribution of GATA motifs. These motifs were most enriched in the PBSC-specific group 1 but were depleted in the ITD-specific group 3 DHSs, providing another indication that ITD1 represents a more mature myeloid cell.

To evaluate the role of STAT5 in shaping the FLT3-ITD-specific epigenetic signature, we integrated the DHS data with the STAT5 ChIP-data from FLT3-ITD+ MV4-11 cells. This analysis revealed STAT5 peaks in the HOXB, *AK2*, *VSTM4/c10orf128*, and *ID1* loci, but not at the above-defined ITD-specific DHSs (Figure S3). Moreover, when STAT5 peaks were plotted alongside the ITD1/PBSC DHS comparison, they were found to be broadly distributed throughout the genome and predominantly in the shared DHS group (Figure S4B). Furthermore, just 249 of the 9,572 STAT5 peaks detected were present within the group of 1,216 ITD-specific DHSs (Figure S4C). These data suggest that STAT5 is binding predominantly at pre-existing DHSs and only plays a minor role in maintaining the FLT3-ITD-specific DHSs. A de novo motif analysis of the STAT5 ChIP peaks identified a STAT consensus motif in 16% of these peaks and further suggested that much of the STAT binding is in association with DHSs containing ETS, RUNX, C/EBP, and AP-1 motifs (Figure S4D).

A parallel analysis of DHSs and motifs associated with 380 ITD-specific promoter-associated DHSs revealed a similar ITD-specific epigenetic and binding motif signature (Figures S4E and S4F). Gene ontology analysis of the genes associated with this group of DHSs also revealed a cell activation signature similar to that seen for genes associated with the distal ITD-specific DHSs (Figure S4G).

RUNX1, AP-1, FOX/E-box, and C/EBP Motifs Are Occupied in ITD-Specific DHSs

Our motif analysis pointed to a major role for RUNX and AP-1 in activating FLT3-ITD-specific DHSs. However, the presence of

Figure 4. FLT3-ITD Mutations Are Associated with a Specific Subset of DHSs

(A–C) Venn diagrams depicting the overlaps between populations of DHSs that are 2-fold upregulated in AML samples compared to PBSCs (FC > 2).

(A) Intersections between ITD1, ITD2, and ITD3.

(B) Intersections between ITD1, ITD2, and WT1, which has a NPM1 mutation.

(C) Intersections between WT2, WT3, and WT5.

(D) Gene ontology analysis of the genes closest to the 1,216 ITD-specific DHSs defined in (A).

(E) Plot of the relationship between the log2 mRNA fold change for genes upregulated in ITD+ AML versus the distance to the nearest ITD-specific DHS for all of the 134 ITD-specific genes (red), and the remainder of the 703 upregulated genes (blue) for genes located within 800 kb of an ITD-specific DHS.

(F and G) Log2 mRNA microarray values (as in Figure S1) (F) and UCSC Genome Browser views for DNase-seq and RUNX1 ChIP-seq data (G) for the ITD-specific genes *SCARA3*, *WDR86*, and *CTSG*/*GZMB*. ITD-specific DHSs are enclosed by red ovals.

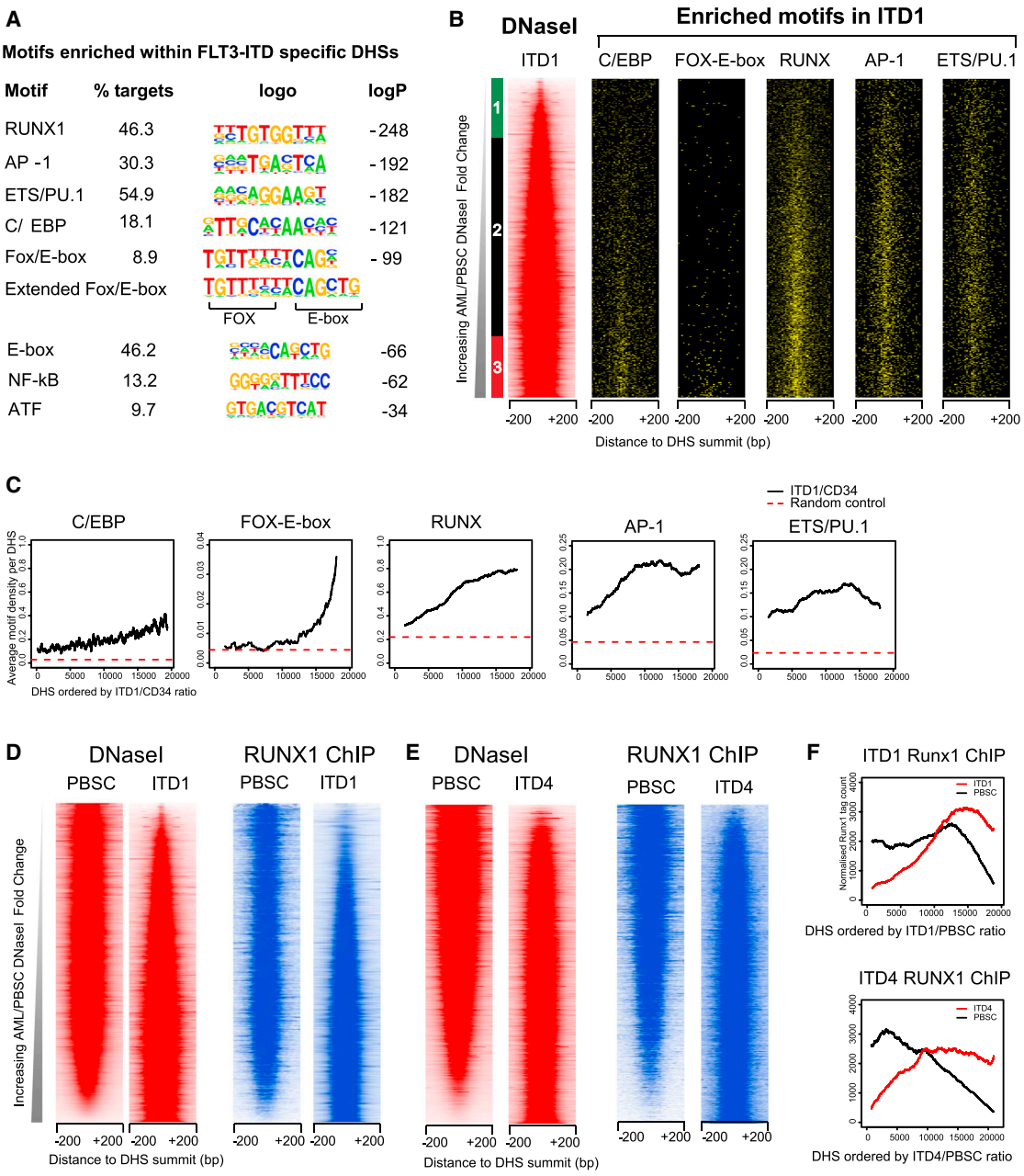

Figure 5. ITD-Specific DHSs Have a Specific Motif Signature and Bind RUNX1

(A) Result of de novo motif search of 1,216 ITD-specific DHSs using HOMER.

(B and C) Alignment of ITD-specific DHS motifs with distal DHSs present in either ITD1 or PBSCs (B) with the rolling averages of motif densities plotted underneath (C).

(D–F) Analysis of RUNX1 ChIP-seq data comparing ITD1 (D), ITD4 (E), and PBSCs (F) plotted alongside the ITD1 and ITD4 DHS data. (F) Depiction of the rolling averages of the ChIP signals.

enriched motifs within specific DHSs does not necessarily mean that they are occupied. To verify occupancy by RUNX1, we performed ChIP-seq assays on ITD1, ITD4, and PBSCs (Figures 5D and 5E). The average profiles of RUNX1 binding (Figure 5F) closely mirrored the distribution of ITD-specific DHSs (Figure S2D) and RUNX motifs (Figure 5C). To account for the increase in RUNX1-bound sites in the ITD+ cells, we examined *RUNX1* expression levels. *RUNX1* expression was elevated in most of the ITD+ AMLs and in the AML with JAK2 mutations compared to normal CD34+ and CD14+ cells, but only in some of the WT FLT3 AMLs (Figure 6A; manual PCR validation shown in Figure S5A). A parallel PCR analysis confirmed that *FOXC1* mRNA was also often upregulated in ITD+ AML (Figure S5B), with both *RUNX1* and *FOXC1* being significantly increased in

each of the core ITD+ group of ITD1, ITD2, and ITD3. The upregulation of *RUNX1* expression may be in part due to the presence of an ITD-specific DHS within the *RUNX1* gene 43 kb downstream of the downstream promoter P2 (Figure 6B), which contains seven motifs linked to ITD-specific DHSs (RUNX, ETS, FOX, AP-1, and E-box) (Figure 6C). These motifs were also seen in the ITD-specific DHSs associated with *FOXC1*, *DSC2*, *AK2*, and *ID1* (Figure S3) and in the *SCARA3*, *CTSG*, *MDGA1*, *MED16*, *GZMB*, VSTM4/*c10orf128*, and *CCNA1* ITD-specific DHSs (Figure S5C). Notable among the 1,216 ITD+ DHSs was a DHS near *C8orf87* containing 5 FOX motifs, one of which was the exact composite FOX/E-box motif defined in Figure 5A. This DHS was 221 kb away from the highly ITD-specific gene *FAM92A1* (Figure S5D). In this case, the gene was again not expressed in AML samples with WT FLT3 unless they carried other mutations in the signaling molecules NRAS or SOCS1 (ITD1 and ITD6, marked by asterisks), or JAK2, and was also not upregulated in samples carrying RUNX1 mutations.

AP-1 is highly relevant to this study because it normally functions as a tightly regulated MAPK-inducible factor known to play major roles in the control of cell growth, survival, and cancer (Shaulian, 2010; Shaulian and Karin, 2002). To test for enhanced AP-1 activity, we used electrophoretic mobility shift assays (EMSAs) to examine the levels of nuclear AP-1 DNA-binding activities in both FLT-ITD+ and WT FLT3 myeloid cell lines (Figure 6D). Both of the ITD+ cell lines MV4-11 and MOLM14 had high levels of constitutive AP-1 activity, equivalent to the induced levels of AP-1 seen in the WT FLT3 cell lines U937 and THP1. Because AP-1 is a MAPK-inducible factor, we also used western blots of MV4-11 cell proteins to look for evidence of FLT3-dependent activation of MAPK signaling pathways (Figure 6E). This analysis revealed FLT3-dependent phosphorylation of both ERK1/2 and RSK2 (which are downstream of RAS signaling), which was suppressed by small interfering RNA (siRNA) directed against FLT3. This confirmed the FLT3-dependent activation not only of MAPK and the STAT pathways but also of STAT5. Furthermore, quantitative RT-PCR analyses revealed suppression of expression of several previously defined ITD-specific genes in MV4-11 cells after treatment with either FLT3 siRNA or a combination of inhibitors directed against the MEK, JNK, and p38 MAPK pathways (Figure 6F). We used ChIP to confirm that one partner of the AP-1 complex, FOS, was bound to four ITD-specific DHSs in MV4-11 cells (Figure 6G) that each contain AP-1 motifs (Figure S5C) and that RUNX1 was also bound to three of these DHSs and to the *CSF1R* FIRE element (Ptasinska et al., 2014) used here as a control for RUNX1 binding. In parallel we demonstrated that either FLT3 siRNA or MAPK inhibitors were sufficient to substantially diminish binding of FOS and RUNX1 to these ITD-specific DHSs, to a greater extent than seen at the FIRE RUNX site (Figure 6G). Last, but not least, we performed a ChIP-seq analysis for FOS in MV4-11 cells treated with FLT3 siRNA, which demonstrated a global decrease in the binding of FOS (Figure 6H). In summary, our data demonstrate that constitutive FLT3-ITD signaling leads to chronic activation of AP-1 via the MAPK pathway, which together with RUNX1 leads to chromatin remodeling and the activation of specific genes.

We next wanted to understand the role of other TFs in shaping ITD-specific DHS and how they would work together. To find additional evidence for the binding of these factors, we employed our recently developed Wellington algorithm that uses DNase-seq data to perform genome-wide in silico DNase I footprinting of regulatory motifs (Piper et al., 2013). This methodology determines statistically whether a given DNA sequence is protected from DNase I digestion, thereby indicating that it is occupied by a TF, as modeled in Figure 7A. Figure 7B depicts the density of upper (red) and lower (green) strand DNase I cleavage sites detected in ITD1 and PBSCs at all 5,142 FLT3-ITD-specific predicted footprints and at the specific subset carrying AP-1 motifs. The black gap between the red and the green signal indicates that the AP-1 motifs were occupied at a high frequency in ITD+ cells, but not in PBSCs. This analysis provided convincing evidence that AP-1 motifs are preferentially occupied in the FLT3-ITD AML sample, even though ITD1 and PBSCs share many DHSs that contain AP-1 motifs. These ITD-specific footprints also included 63 STAT5 motifs and 226 STAT4 motifs (some of which will be the same motif), but none of these were associated with any of the 134 or 77 FLT3-ITD-specific upregulated or downregulated genes.

A de novo search for motifs within the 5,142 footprints revealed essentially the same signature as that of the 1,216 ITD-specific DHSs (Figure 7C), but with an additional motif for Nuclear Factor 1 (NF1) that may be linked to the ITD-specific upregulation of *NF1X*, which contains an ITD-specific DHS occupied by RUNX1 (data not shown). Figure 7D depicts the locations of the footprinted ITD-specific motifs on the ITD1/PBSC DHS coordinates displayed above in Figures 3E and 5B, demonstrating a close alignment with the DHS peak summits and with the FOX/E-box, C/EBP, and NF-κB motifs each being preferentially occupied in the ITD-specific DHSs. Occupied AP-1 motifs were equally distributed between ITD1-specific DHSs and DHSs shared with PBSCs, indicating constitutive binding of AP-1 to the shared sites in FLT3-ITD AML. We confirmed the existence of footprints at many of the predicted protected motifs by plotting the frequency of DNase I cleavage on the upper and lower strand in ITD1, alongside the footprint probability profiles and the motifs in Figure S6A. The parallel analysis of footprints in ITD2 showed similar results (not shown). To confirm the ability of our algorithm to detect STAT footprints, we show a footprint spanning the STAT motif, plus a second footprint spanning ETS and AP-1 motifs within the *ID1* +5 kb DHS in ITD1 (Figure S6B). Overall, these results highlight (1) that gene activation in ITD+ AML involves FLT3-ITD-driven constitutive binding of normally inducible factors to pre-existing DHSs and (2) that RUNX1 and AP-1 are associated with both pre-existing and ITD-specific DHSs.

To examine, whether TFs binding to ITD-specific DHSs function in cooperation, we performed a bootstrapping analysis to identify which specific footprinted motifs were co-localized with 50 bp of each other (Figure 7E). This revealed a strong co-association of the occupied FOX, E-box, C/EBP, RUNX1, and AP-1 motifs within the same DHSs. Curiously, the ETS motifs were not preferentially footprinted in the ITD-specific DHSs, and they did not co-localize with the other ITD-specific motifs, which may tie in with the finding that PU.1 activity is downregulated in FLT3-ITD (Gerloff et al., 2015). In summary, these analyses demonstrate that the establishment of FLT3-ITD-specific

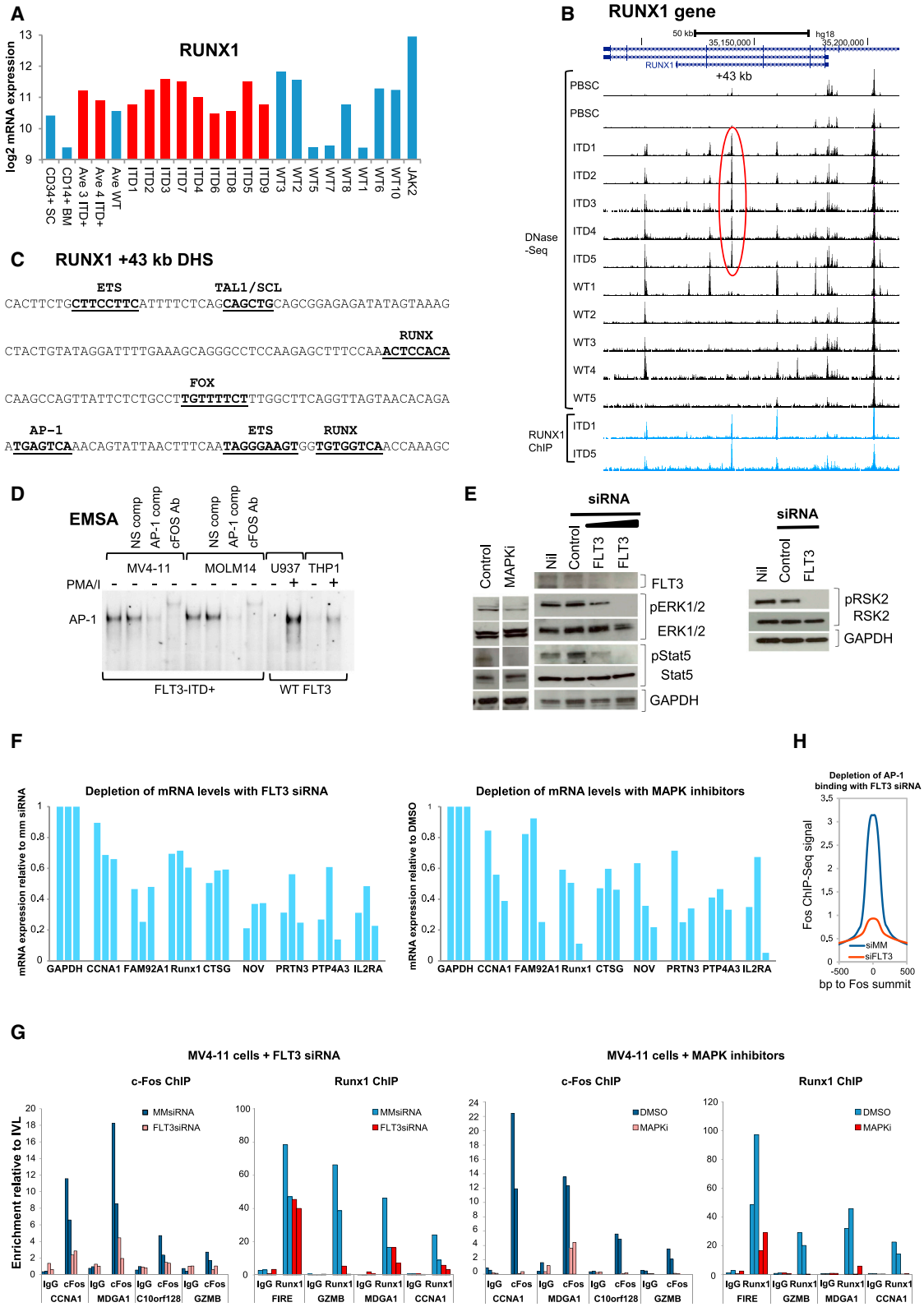

Figure 6. AP-1 and RUNX Pathways Are Activated in ITD+ AML

(A) Log2 *RUNX1* mRNA microarray values.

(B) UCSC Genome Browser view for RUNX1 DNase-seq.

(legend continued on next page)

DHSs is mediated by the interaction of a limited set of constitutive and inducible transcription factors.

DISCUSSION

A two-hit model of leukemogenesis is commonly accepted whereby a mutation in a transcriptional or epigenetic regulator gene impacting on gene expression and differentiation (class II mutation) cooperates with a mutation in a gene such as a signaling molecule regulating growth (class I mutation) (Renneville et al., 2008). Here we show at the systems level, in primary cells from patients, that this distinction is becoming blurred, with signaling having wide-ranging impacts on gene expression. Our study uncovers a significant role for chronic signaling by a mutated FLT3 growth factor receptor to the nucleus and demonstrates a profound impact of aberrant signaling on transcription factor binding and FLT3-ITD-specific gene expression. Our findings are consistent with the model depicted in Figure 7F in which aberrant FLT3-signaling activates both STAT and MAPK signaling. The latter, via the activation of inducible transcription factors such as AP-1/ATF family members and NF-κB, upregulates genes such as *RUNX1* and *FOXC1*, which in cooperation with other factors, including C/EBP, ETS, and E-box family members, activate specific *cis*-regulatory elements driving the expression of many target genes. A similar cooperation between RUNX1 and AP-1 in response to MAPK signaling has been seen during megakaryocyte differentiation (Pencovich et al., 2011). Moreover, our mutation data indicate that alternate mutation of another member of the MAPK pathway (NRAS) may upregulate related sets of *cis*-regulatory elements. Furthermore, the mutation of RUNX1 disturbs the FLT3-ITD-specific expression pattern and may also influence the expression of the *FOXC1* gene, which is not highly expressed in the patient containing mutant RUNX1 (ITD9) (Figure S1A). *FOXC1* is itself linked to an ITD-specific DHS that contains three RUNX consensus motifs and that binds RUNX1 in ITD1 (Figure S3A).

A surprise finding from our study was the absence of enriched STAT motifs in our global analysis of ITD-specific DHSs in spite of overwhelming evidence (also from this study) that FLT3-ITD feeds into the STAT pathway and is required for enhanced translocation of STAT5 into the nucleus and leukemic survival (Chatterjee et al., 2014; Gu et al., 2011; Masson and Rönnstrand, 2009; Mizuki et al., 2000; Zhang et al., 2000). Furthermore, the data from MV4-11 cells suggested that STAT5 is bound predominantly at pre-existing DHSs that are shared with CD34+ cells, not STAT5-dependent DHSs, and thus is not involved in opening up additional FLT3-ITD-dependent DHSs. It is also possible that STAT5 binding to its targets may be only be required for the upregulation of a limited set of survival genes (such as *MYC* or *BCLXL*) (Chatterjee et al., 2014) and so is simply not present at most ITD-specific DHSs. In contrast, AP-1 may interact with many more ITD-specific targets. It is known that AP-1 regulates the inflammatory response and is involved in activating gene expression in multiple types of cancers with an inflammatory phenotype such as breast cancer, melanoma, and Hodgkin's lymphoma (Giancotti, 2006; Kappelmann et al., 2014; Kreher et al., 2014). We previously showed that the chronic activation of regulators of inflammatory response genes such as *JUN* and *IRF5* activates a Hodgkin's lymphoma-specific gene expression program characterized by cytokine and chemokine expression, which during disease progression is progressively upregulated by chronic autocrine and paracrine stimulation (Kreher et al., 2014). It is therefore possible that STAT5 interaction with DNA is required for the initiation of the leukemic phenotype, but during leukemia development in patients it becomes less important due to the progressive establishment of a FLT3-ITD-specific transcriptional network that is driven by chronic inflammation and MAPK responsive transcription factors. This feature is consistent with our finding of the FLT3-ITD-specific upregulation of inflammatory response genes, such as chemokine genes, growth factor receptor genes, and genes involved in leukocyte activation and response to bacterial stimuli.

The FLT3-ITD mutation comes with a bad prognosis, and attempts to cure this type of AML using FLT3 inhibitors have met with only limited success (Grundler et al., 2003; Levis et al., 2011). Our system-wide studies of primary cells highlighting a common MAPK-responsive transcriptional network are therefore of utmost importance for cancer therapy, which may be applicable to ITD+ AML. Efforts to evaluate the role of different genes within this network with respect to the maintenance of the leukemogenic phenotype are currently underway.

EXPERIMENTAL PROCEDURES

Detailed methods are in the Supplemental Information.

Patient Samples

AML cells and PBSCs were purified by density gradient centrifugation. Where the blasts were less than 92%, cells were further purified using CD34 or CD117 antibody coupled beads.

DNase-Seq and ChIP-Seq

Global analyses of DHSs and RUNX1 binding, and data analyses, were performed as in Ptasinska et al. (2014).

(C) Sequence of the ITD-specific *RUNX1* +43-kb DHS with the indicated sequence motifs underlined, which underlay the ITD-specific DHS signature.
(D) EMSA using nuclear extracts from the indicated cell lines grown in the presence and absence of stimulation for 2 hr with phorbol 12-myristate 13-acetate and calcium ionophore A23187 (PMA/I) to induce AP-1 activity. Some assays include AP-1 or non-specific (NS) DNA competitors or FOS antibodies.
(E) Western blot analyses extracts from ITD+ MV4-11 cells treated with FLT3 or mismatch (MM) control siRNA, using the indicated antibodies.
(F) RT-QPCR analysis of ITD target gene mRNA expression after treatment of MV4-11 cells with either siRNA against FLT3 (left) or with the MAPK pathway inhibitors PD98059, SP600125, and SB202190 directed against MEK1/2, JNK, and p38, respectively (right), from three independent experiments for each gene. Values were calculated relative to *GAPDH*.
(G) ChIP analyses of FOS and RUNX1 binding to ITD-specific DHSs, with normal IgG used as a control. Data are expressed relative to FOS or RUNX1 binding to a region in the inactive *IVL* locus.
(H) Average FOS ChIP peak profiles obtained from MV4-11 cells treated with either FLT3 or MM siRNA.

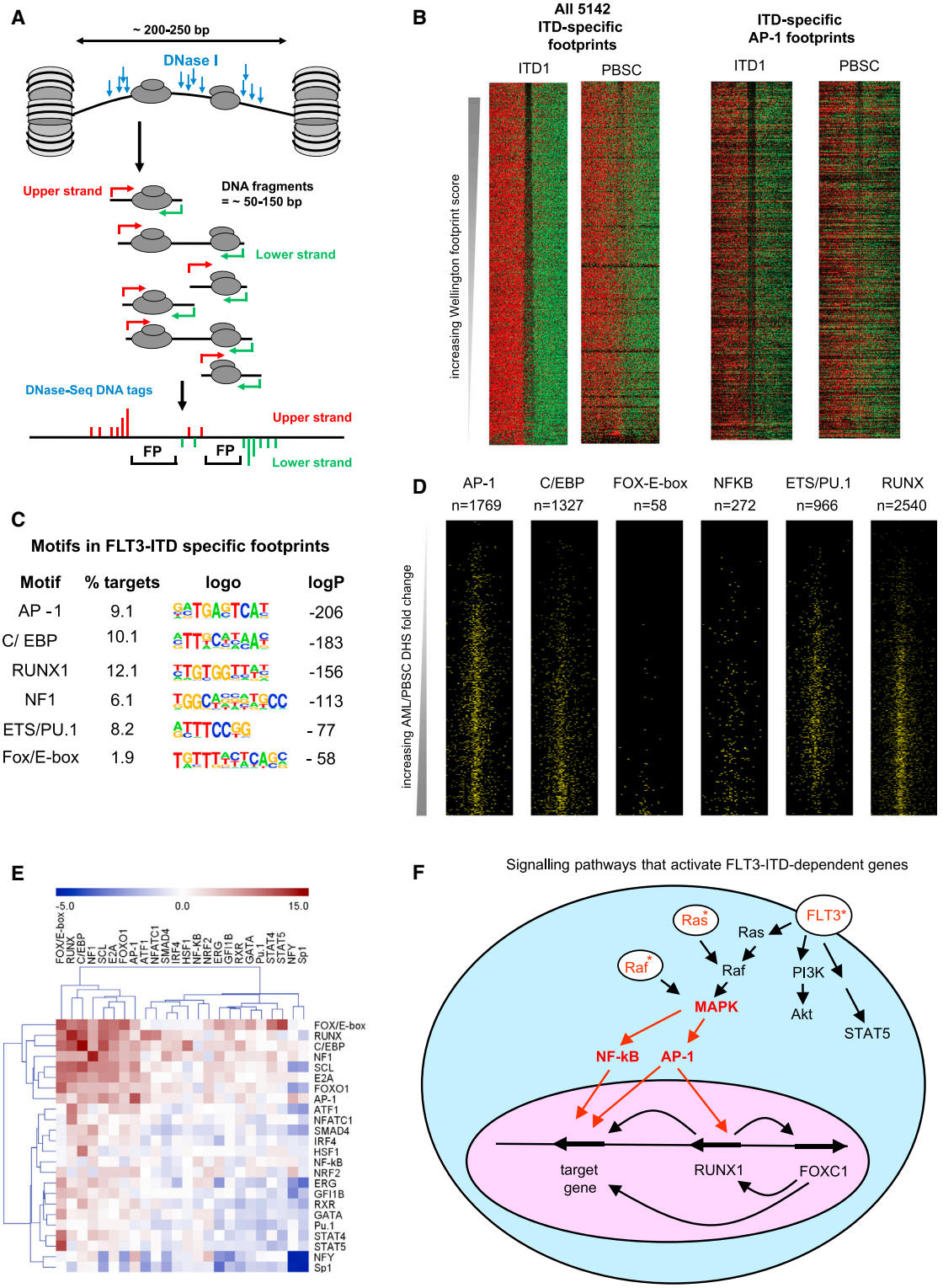

Figure 7. ITD-Specific DHS Motifs Are Occupied in ITD+ AML

(A) Model depicting the generation of DNase I footprints at DHSs.

(B) DNase I cleavage patterns within ITD1-specific footprints predicted by Wellington. Upper strand cut sites are shown in red and lower strand cut sites in green within a 200-bp window centered on each footprint (gap), for all 5,142 ITD-specific footprints, and for those containing AP-1 sites.

(legend continued on next page)

Mutations

Screening of DNA for mutations in the 55 AML-associated genes listed in Data File S1 was performed by WMRGL, Birmingham Women's Hospital.

DNA Methylation

Analyses of DNA methylation were performed by Gen-Probe using the Illumina 450K platform.

ACCESSION NUMBERS

The DNase-seq, ChIP-seq, and mRNA array data reported in this study are available in the Gene Expression Omnibus (http://www.ncbi.nlm.nih.gov/geo/) as a superseries under the accession number GEO:GSE64874.

SUPPLEMENTAL INFORMATION

Supplemental Information includes Supplemental Experimental Procedures, six figures, one table, and three data files and can be found with this article online at http://dx.doi.org/10.1016/j.celrep.2015.06.069.

AUTHOR CONTRIBUTIONS

P.N.C., C.B., and P.C. wrote the paper. P.N.C., C.B., P.C., S.R.J., A.P., J.Z.-C., M.R.I., S.A.A., J.P., M.C., M.H., D.R.W., and S.O. designed and performed the experiments and analyzed the results. P.N.C., C.B., S.A., S.J.C., and M.J.G. coordinated and analyzed the mutation analyses. M.R., J.L., M.J.G., and S.J.R. obtained patent samples and analyzed patient data.

ACKNOWLEDGMENTS

We would like to thank A. Jack, C. Craddock, A. Lubenko, R. Tooze, J. Burrow, J. Jesson, P. Jenkin, and D. Hollyman for help obtaining samples, D. Tenen and M. Wu for help with DNA sequencing, K. Keeshan, P. Twiss, and A. Rettino for help with mutation analyses, and S. Kissane for microarray analyses. This research was funded by a Specialist Programme Grant from Leukaemia Lymphoma Research to P.N.C. and C.B., the Kay Kendall Leukemia Fund, and an EPSRC studentship for J.P.

Received: January 13, 2015
Revised: May 20, 2015
Accepted: June 19, 2015
Published: July 23, 2015

REFERENCES

Badeaux, A.I., and Shi, Y. (2013). Emerging roles for chromatin as a signal integration and storage platform. Nat. Rev. Mol. Cell Biol. *14*, 211–224.

Bernstein, B.E., Stamatoyannopoulos, J.A., Costello, J.F., Ren, B., Milosavljevic, A., Meissner, A., Kellis, M., Marra, M.A., Beaudet, A.L., Ecker, J.R., et al. (2010). The NIH Roadmap Epigenomics Mapping Consortium. Nat. Biotechnol. *28*, 1045–1048.

Cancer Genome Atlas Research Network (2013). Genomic and epigenomic landscapes of adult de novo acute myeloid leukemia. N. Engl. J. Med. *368*, 2059–2074.

Chatterjee, A., Ghosh, J., Ramdas, B., Mali, R.S., Martin, H., Kobayashi, M., Vemula, S., Canela, V.H., Waskow, E.R., Visconte, V., et al. (2014). Regulation of Stat5 by FAK and PAK1 in oncogenic FLT3- and KIT-driven leukemogenesis. Cell Rep. *9*, 1333–1348.

Cockerill, P.N. (2011). Structure and function of active chromatin and DNase I hypersensitive sites. FEBS J. *278*, 2182–2210.

Corces-Zimmerman, M.R., and Majeti, R. (2014). Pre-leukemic evolution of hematopoietic stem cells: the importance of early mutations in leukemogenesis. Leukemia *28*, 2276–2282.

Corces-Zimmerman, M.R., Hong, W.J., Weissman, I.L., Medeiros, B.C., and Majeti, R. (2014). Preleukemic mutations in human acute myeloid leukemia affect epigenetic regulators and persist in remission. Proc. Natl. Acad. Sci. USA *111*, 2548–2553.

Dawson, M.A., Bannister, A.J., Göttgens, B., Foster, S.D., Bartke, T., Green, A.R., and Kouzarides, T. (2009). JAK2 phosphorylates histone H3Y41 and excludes HP1alpha from chromatin. Nature *461*, 819–822.

de Pater, E., Kaimakis, P., Vink, C.S., Yokomizo, T., Yamada-Inagawa, T., van der Linden, R., Kartalaei, P.S., Camper, S.A., Speck, N., and Dzierzak, E. (2013). Gata2 is required for HSC generation and survival. J. Exp. Med. *210*, 2843–2850.

Gerloff, D., Grundler, R., Wurm, A.A., Brauer-Hartmann, D., Katzerke, C., Hartmann, J.U., Madan, V., Muller-Tidow, C., Duyster, J., Tenen, D.G., et al. (2015). NF-κB/STAT5/miR-155 network targets PU.1 in FLT3-ITD-driven acute myeloid leukemia. Leukemia *29*, 535–547.

Giancotti, V. (2006). Breast cancer markers. Cancer Lett. *243*, 145–159.

Goyama, S., Huang, G., Kurokawa, M., and Mulloy, J.C. (2014). Posttranslational modifications of RUNX1 as potential anticancer targets. Oncogene *34*, 3483–3492.

Grundler, R., Thiede, C., Miething, C., Steudel, C., Peschel, C., and Duyster, J. (2003). Sensitivity toward tyrosine kinase inhibitors varies between different activating mutations of the FLT3 receptor. Blood *102*, 646–651.

Gu, T.L., Nardone, J., Wang, Y., Loriaux, M., Villén, J., Beausoleil, S., Tucker, M., Kornhauser, J., Ren, J., MacNeill, J., et al. (2011). Survey of activated FLT3 signaling in leukemia. PLoS ONE *6*, e19169.

Heinz, S., Benner, C., Spann, N., Bertolino, E., Lin, Y.C., Laslo, P., Cheng, J.X., Murre, C., Singh, H., and Glass, C.K. (2010). Simple combinations of lineage-determining transcription factors prime *cis*-regulatory elements required for macrophage and B cell identities. Mol. Cell *38*, 576–589.

Heinz, S., Romanoski, C.E., Benner, C., Allison, K.A., Kaikkonen, M.U., Orozco, L.D., and Glass, C.K. (2013). Effect of natural genetic variation on enhancer selection and function. Nature *503*, 487–492.

Kappelmann, M., Bosserhoff, A., and Kuphal, S. (2014). AP-1/c-Jun transcription factors: regulation and function in malignant melanoma. Eur. J. Cell Biol. *93*, 76–81.

Kreher, S., Bouhlel, M.A., Cauchy, P., Lamprecht, B., Li, S., Grau, M., Hummel, F., Köchert, K., Anagnostopoulos, I., Jöhrens, K., et al. (2014). Mapping of transcription factor motifs in active chromatin identifies IRF5 as key regulator in classical Hodgkin lymphoma. Proc. Natl. Acad. Sci. USA *111*, E4513–E4522.

Levis, M., Ravandi, F., Wang, E.S., Baer, M.R., Perl, A., Coutre, S., Erba, H., Stuart, R.K., Baccarani, M., Cripe, L.D., et al. (2011). Results from a randomized trial of salvage chemotherapy followed by lestaurtinib for patients with FLT3 mutant AML in first relapse. Blood *117*, 3294–3301.

Martens, J.H., Mandoli, A., Simmer, F., Wierenga, B.J., Saeed, S., Singh, A.A., Altucci, L., Vellenga, E., and Stunnenberg, H.G. (2012). ERG and FLI1 binding sites demarcate targets for aberrant epigenetic regulation by AML1-ETO in acute myeloid leukemia. Blood *120*, 4038–4048.

Masson, K., and Rönnstrand, L. (2009). Oncogenic signaling from the hematopoietic growth factor receptors c-Kit and Flt3. Cell. Signal. *21*, 1717–1726.

Mizuki, M., Fenski, R., Halfter, H., Matsumura, I., Schmidt, R., Müller, C., Grüning, W., Kratz-Albers, K., Serve, S., Steur, C., et al. (2000). Flt3 mutations from patients with acute myeloid leukemia induce transformation of 32D cells mediated by the Ras and STAT5 pathways. Blood *96*, 3907–3914.

(C) Analysis of overrepresented binding motifs within each footprint using HOMER.
(D) Profiles of motifs in ITD-specific footprints plotted on the same DHS axes as used in Figure 2E.
(E) Analysis of statistically significant co-localization of the indicated footprinted motifs within 50 bp of each other using bootstrapping analysis (*Z* score).
(F) Model of an ITD-specific transcriptional network based on our data.

Pencovich, N., Jaschek, R., Tanay, A., and Groner, Y. (2011). Dynamic combinatorial interactions of RUNX1 and cooperating partners regulates megakaryocytic differentiation in cell line models. Blood *117*, e1–e14.

Piper, J., Elze, M.C., Cauchy, P., Cockerill, P.N., Bonifer, C., and Ott, S. (2013). Wellington: a novel method for the accurate identification of digital genomic footprints from DNase-seq data. Nucleic Acids Res *41*, e201.

Prange, K.H., Singh, A.A., and Martens, J.H. (2014). The genome-wide molecular signature of transcription factors in leukemia. Exp. Hematol. *42*, 637–650.

Ptasinska, A., Assi, S.A., Mannari, D., James, S.R., Williamson, D., Dunne, J., Hoogenkamp, M., Wu, M., Care, M., McNeill, H., et al. (2012). Depletion of RUNX1/ETO in t(8;21) AML cells leads to genome-wide changes in chromatin structure and transcription factor binding. Leukemia *26*, 1829–1841.

Ptasinska, A., Assi, S.A., Martinez-Soria, N., Imperato, M.R., Piper, J., Cauchy, P., Pickin, A., James, S.R., Hoogenkamp, M., Williamson, D., et al. (2014). Identification of a dynamic core transcriptional network in t(8;21) AML that regulates differentiation block and self-renewal. Cell Rep. *8*, 1974–1988.

Ray, D., Kwon, S.Y., Ptasinska, A., and Bonifer, C. (2013). Chronic growth factor receptor signaling and lineage inappropriate gene expression in AML: the polycomb connection. Cell Cycle *12*, 2159–2160.

Reddy, P.N., Sargin, B., Choudhary, C., Stein, S., Grez, M., Müller-Tidow, C., Berdel, W.E., Serve, H., and Brandts, C.H.; Study Alliance Leukemia (SAL) (2012). SOCS1 cooperates with FLT3-ITD in the development of myeloproliferative disease by promoting the escape from external cytokine control. Blood *120*, 1691–1702.

Renneville, A., Roumier, C., Biggio, V., Nibourel, O., Boissel, N., Fenaux, P., and Preudhomme, C. (2008). Cooperating gene mutations in acute myeloid leukemia: a review of the literature. Leukemia *22*, 915–931.

Sallmyr, A., Fan, J., Datta, K., Kim, K.T., Grosu, D., Shapiro, P., Small, D., and Rassool, F. (2008). Internal tandem duplication of FLT3 (FLT3/ITD) induces increased ROS production, DNA damage, and misrepair: implications for poor prognosis in AML. Blood *111*, 3173–3182.

Scholl, C., Gilliland, D.G., and Fröhling, S. (2008). Deregulation of signaling pathways in acute myeloid leukemia. Semin. Oncol. *35*, 336–345.

Shaulian, E. (2010). AP-1—The Jun proteins: oncogenes or tumor suppressors in disguise? Cell. Signal. *22*, 894–899.

Shaulian, E., and Karin, M. (2002). AP-1 as a regulator of cell life and death. Nat. Cell Biol. *4*, E131–E136.

Stirewalt, D.L., and Radich, J.P. (2003). The role of FLT3 in haematopoietic malignancies. Nat. Rev. Cancer *3*, 650–665.

Tam, W.F., Gu, T.L., Chen, J., Lee, B.H., Bullinger, L., Fröhling, S., Wang, A., Monti, S., Golub, T.R., and Gilliland, D.G. (2008). Id1 is a common downstream target of oncogenic tyrosine kinases in leukemic cells. Blood *112*, 1981–1992.

Thiede, C., Steudel, C., Mohr, B., Schaich, M., Schäkel, U., Platzbecker, U., Wermke, M., Bornhäuser, M., Ritter, M., Neubauer, A., et al. (2002). Analysis of FLT3-activating mutations in 979 patients with acute myelogenous leukemia: association with FAB subtypes and identification of subgroups with poor prognosis. Blood *99*, 4326–4335.

Verhaak, R.G., Wouters, B.J., Erpelinck, C.A., Abbas, S., Beverloo, H.B., Lugthart, S., Löwenberg, B., Delwel, R., and Valk, P.J. (2009). Prediction of molecular subtypes in acute myeloid leukemia based on gene expression profiling. Haematologica *94*, 131–134.

Wilson, N.K., Foster, S.D., Wang, X., Knezevic, K., Schütte, J., Kaimakis, P., Chilarska, P.M., Kinston, S., Ouwehand, W.H., Dzierzak, E., et al. (2010). Combinatorial transcriptional control in blood stem/progenitor cells: genome-wide analysis of ten major transcriptional regulators. Cell Stem Cell *7*, 532–544.

Wolf, S., Rudolph, C., Morgan, M., Büsche, G., Salguero, G., Stripecke, R., Schlegelberger, B., Baum, C., and Modlich, U. (2013). Selection for Evi1 activation in myelomonocytic leukemia induced by hyperactive signaling through wild-type NRas. Oncogene *32*, 3028–3038.

Wood, A.D., Chen, E., Donaldson, I.J., Hattangadi, S., Burke, K.A., Dawson, M.A., Miranda-Saavedra, D., Lodish, H.F., Green, A.R., and Göttgens, B. (2009). ID1 promotes expansion and survival of primary erythroid cells and is a target of JAK2V617F-STAT5 signaling. Blood *114*, 1820–1830.

Yordy, J.S., and Muise-Helmericks, R.C. (2000). Signal transduction and the Ets family of transcription factors. Oncogene *19*, 6503–6513.

Zaret, K.S., and Carroll, J.S. (2011). Pioneer transcription factors: establishing competence for gene expression. Genes Dev. *25*, 2227–2241.

Zhang, S., Fukuda, S., Lee, Y., Hangoc, G., Cooper, S., Spolski, R., Leonard, W.J., and Broxmeyer, H.E. (2000). Essential role of signal transducer and activator of transcription (Stat)5a but not Stat5b for Flt3-dependent signaling. J. Exp. Med. *192*, 719–728.

Cell Reports

Supplemental Information

Chronic FLT3-ITD Signaling in Acute Myeloid Leukemia Is Connected to a Specific Chromatin Signature

Pierre Cauchy, Sally R. James, Joaquin Zacarias-Cabeza, Anetta Ptasinska, Maria Rosaria Imperato, Salam A. Assi, Jason Piper, Martina Canestraro, Maarten Hoogenkamp, Manoj Raghavan, Justin Loke, Susanna Akiki, Samuel J. Clokie, Stephen J. Richards, David R. Westhead, Michael J. Griffiths, Sascha Ott, Constanze Bonifer, and Peter N. Cockerill

Table S1: List of genes screened for mutations

	Gene	mutations found	Region of Interest
Epigenetic	ASXL1	2	1/1, exon 13
	BCOR	3	8/14 exons, 4,5,8,9,11,12,14,15
	BCORL1	2	7/12 exons, 2,3,4,5,7,8,11
	CREBBP		25/31 exons 2,5,6,8,10-18,20-31
	DNMT3A	5	21/23 exons 3-23(NM_175629,NM_022552)
	EZH2		19/20 exons 2-20(NM_001203248)
	IDH1	3	exon 4 (R132)
	IDH2	2	exon 4 (R140)
	KDM6A (UTX)		19/29 exons 1,4,6,8,10,12,16-28
	MLL		13/36 exons 3,5,7,11,15,16,21,22,25,26,27,33,35
	SUZ12		4/16 exons 2,3,5,16
	TET2	7	9/9 exons 1-9
Chromatin Remodelling	ATRX		23/34 exons 1,4,7,9,11-15,17-23,25,26,28,29,31-33
	DAXX		7/8 exons 2,3,4,5,6,7,8
	H3F3A (H3.3)		exon 1 Codons K27M/G34R
Cell Cycle	CDKN2A (p16)		3/3 exons
Signalling	GNAS		amino acid R201/Q227
	HRAS		exons 2,3,4
	JAK2	2	exon 12, 14 (V617F)
	KRAS		exons 2,3,4
	MPL		exon 10 (W515K)
	NF1		58/58 exons 1-58
	NPM1	7	exons 11,12
	NRAS	1	exons 2,3,4
	PTEN		9/9 exons
	RASSF1		2/5 exons 4,5 (NM_170713)
	SH2B3 (LNK)		2/7 exons 5,6,(NM-005475)
	CTNNB1 (B-catenin)		codon Y654
	SOCS1	1	1/1 exon 1
	PTPN11	1	3,13,Y197(ex5)
Transcription Factor	CEBPa	4	1/1 exon 1
	ETV6		5/8 exons 2,3,5,6,7
	GATA1		3/6 exons 2,3,6
	GATA2	3	5/6 exons 2-6 (NM_032638)
	IKZF1		4/8 exons 2,4,6,8 (NM_006060)
	MAFB		1/1 exon 1
	PHF6	1	4/11 exons 2,7,8,9
	RUNX1	5	6/8 exons 3-8 (NM_001754)
	SPI1 (PU.1)		3/5 exons 3,4,5
	TP53	1	10/10 exons 1-10
	WT1	5	7,9,R430(ex8)
Receptor	KIT		exons 8,9,11,10,13, 17
	EGFR		exons 1-7, 18-22
	NOTCH-1		exon 26,27,34
	PDGFRA		exons 4,6,10
	FLT3	9	exon 14, 15, 20
Splisosome	PRPF40B		10/25 exons 1,2,4,7,12,13,14,17,20,22
	SF1		6/14 exons 2,4,6,7,8,9 (NM_001178030)
	SF3A1		8/16 exons 2-6,10,11,14
	SF3B1		12/25 exons 6,8,11,12,13,14,16,17,18,21,24
	SRSF2	3	amino acid P95
	U2AF1(35)		exons 2,6 (codons 34, 157)
	U2AF2(65)		3/12 exons 5,6,8
	ZRSR2		7/11 exons 1,3,4,7,8,9,11
Ubiquitination	CBL		2/16 exons 8,9

1212 amplicons

Supplemental Figure S1

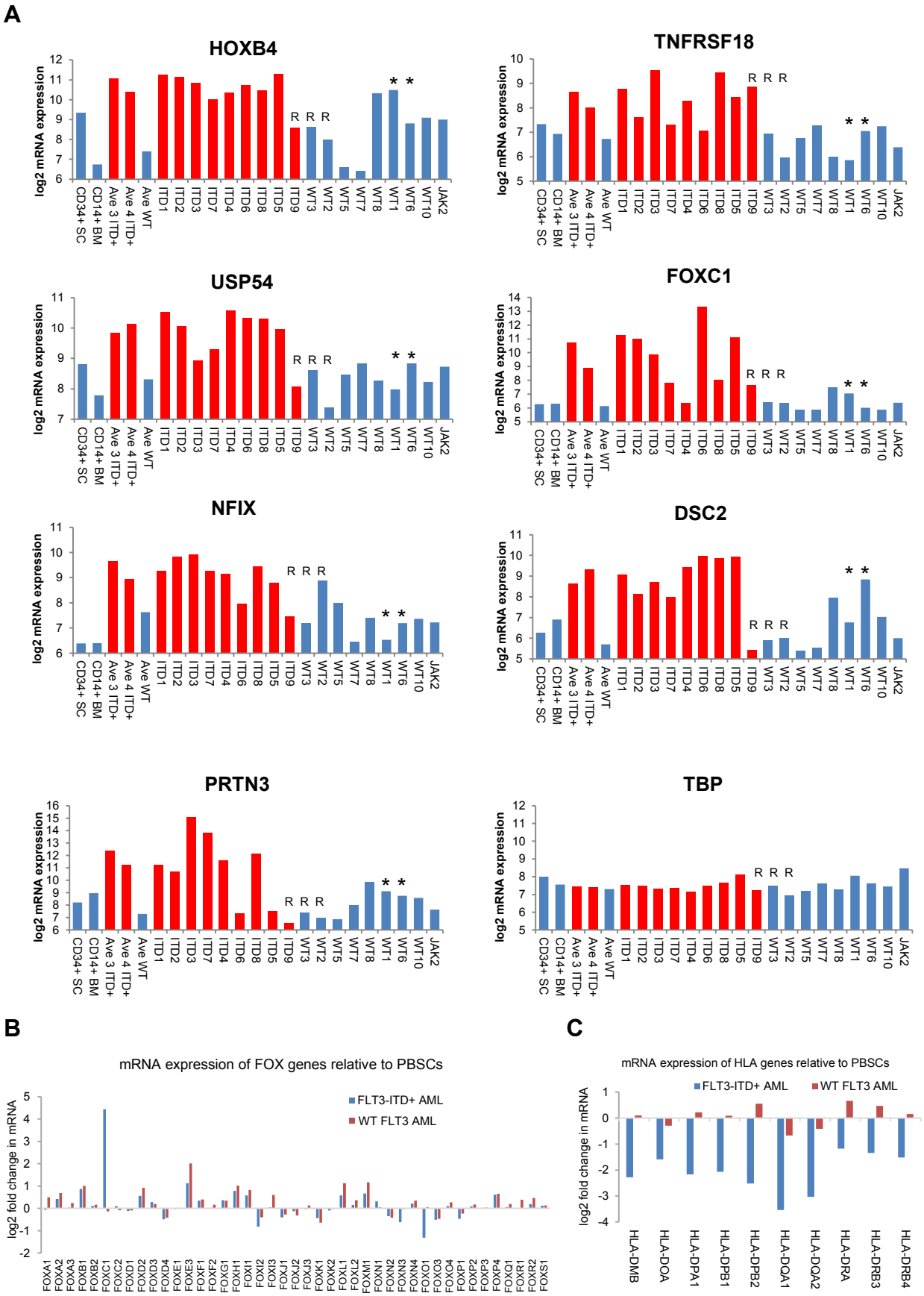

Supplemental Figure 2

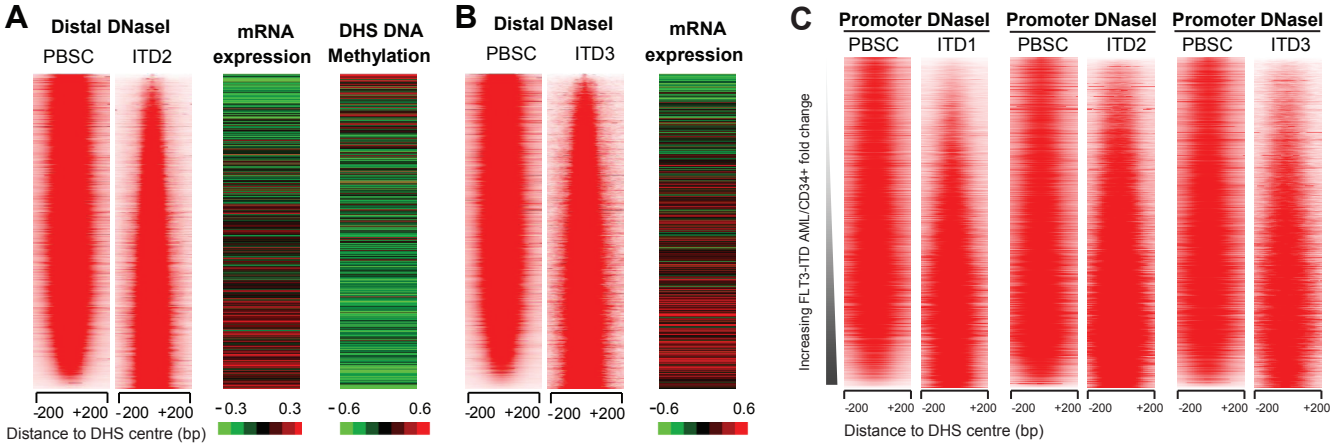

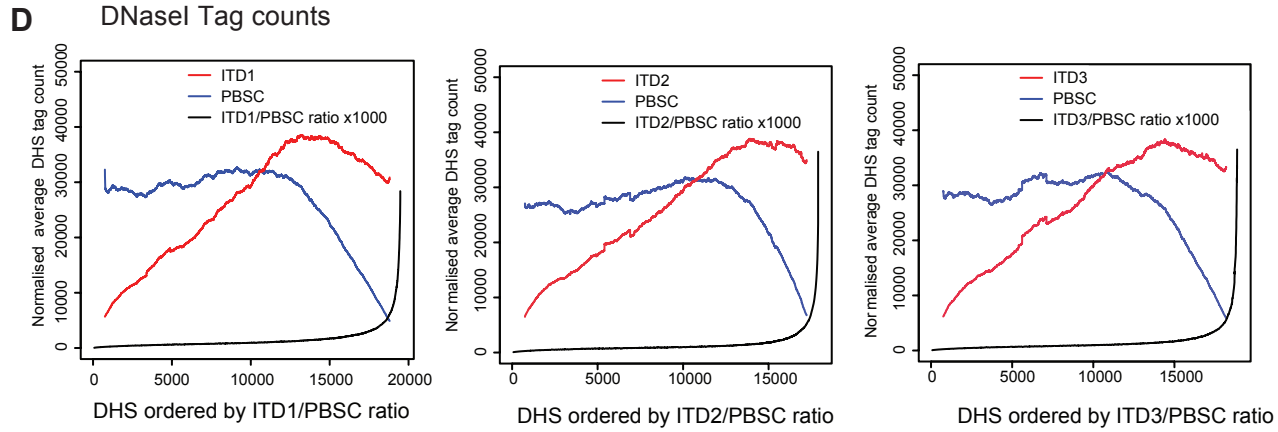

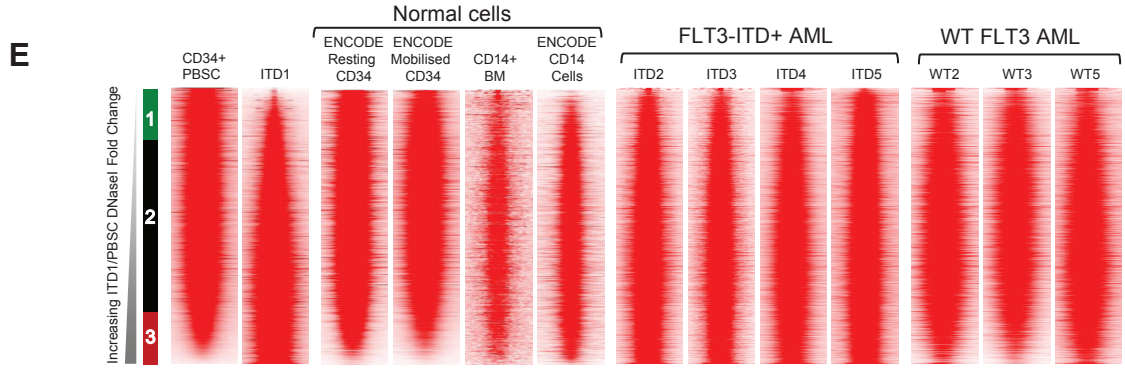

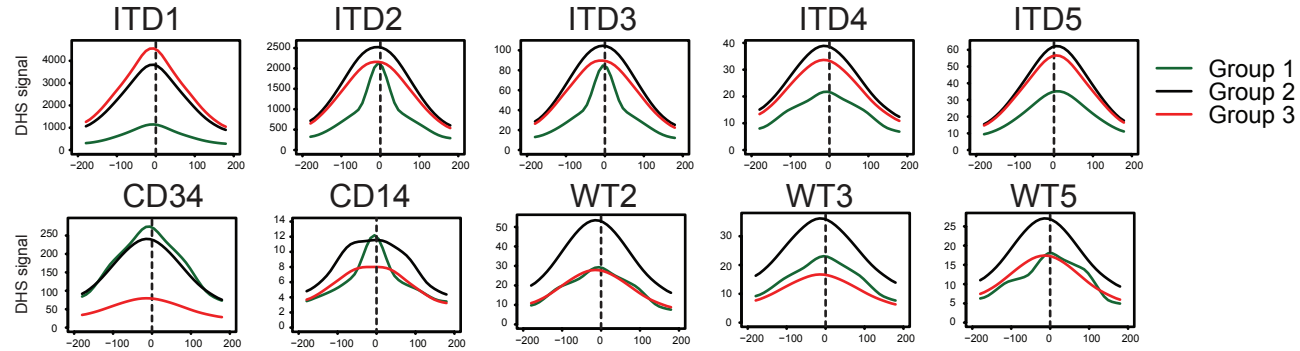

Supplemental Figure S3

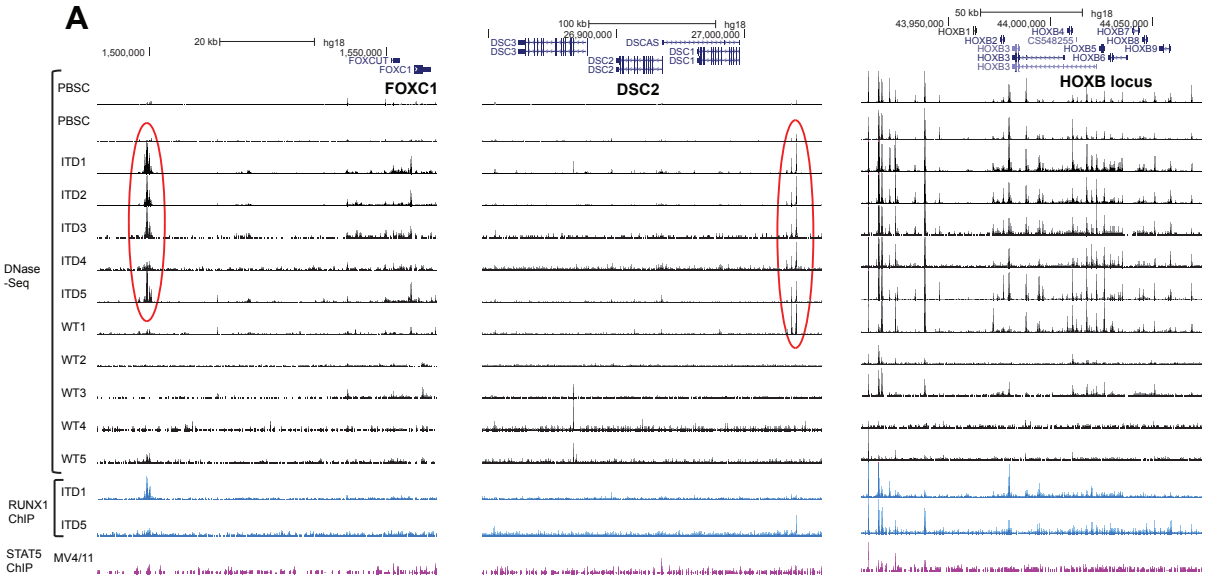

FOXC1 DHS

RUNX
TGTCTACTTACTGGCTT**TGTGGAGT**ATTAAAAAGCACTGCCCAGGGAACCTATTTG
RUNX
CTGG**TGTGGGTT**ATGCCAGGGGTGTCACGGTTTTAGAGTTGGCAGCACTAGCAGTA

GCTTTCGGCTTGGGGGAGTTTCTTGACTATATCAATTGCCTGTCATGGTGGTTTCC
RUNX
GACCCGGGCAGGTGGCATGGTTCTGGGGCTAGCAGC**TGTGGCCA**CCGTTTCCCTAC

DSC2 DHS

AP-1 AP-1 RUNX ETS
TCGG**TGAGTAA**TGCAG**TGACTAAAGCCCACA**CAA**AAAGGAAGC**AGTGCCC
RUNX
TTTTAATA**GAGCCACA**ATATAAAGAAAACACTCAAGCCAGTTCCAGCTAC

TGTGAATGATTTATTGGGTGAGCCCTGCCCGACTAGGCCCAGCAATTTCC
RUNX
CATTTGTTGCGTCCCAATCCTGCCC**CTCCCACA**TCTCCACCCTCCTGCTG

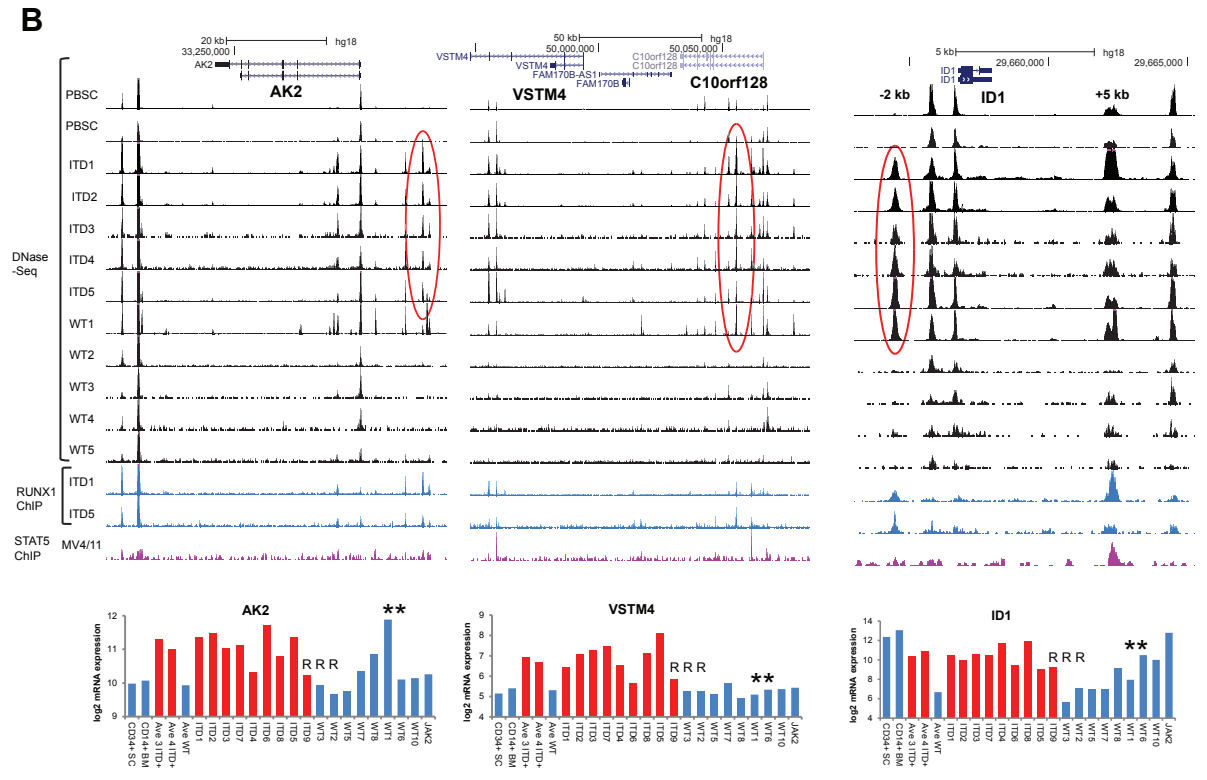

AK2 DHS

ETS
TGTCTTTTTTTGGGCTTCACAGCCCACTTGACCTAGGACC**GCTTCCCAA**T
ETS RUNX
TTTTGTAACAT**GCTTCCTGT**TCCTTTGTCAACC**AAACCACA**ACCATGAGA
RUNX
TGTGGTTTCTAAAGAACTGGCTAAGTCCAAGCCACCTGAACAAGCAAAG
CREB/ATF RUNX
CCTTTCTACTACTGTTT**TGAGGTCA**C**TGTGGCGA**AATTCCGATTTCCATA

ID1 -2 kb DHS

RUNX AP-1
GCACAGATTTTTACCCCTGCTAATGTTG**TGTGG**CTTTGGG**TGACTAA**TCT
RUNX
GAGCTTCGGTTTCCCCACC**TGTGG**CATGTCCAGGACTCTGCAGTCAGACT
ETS C/EBP
GCCTGCTCTCA**GCAGGAAGC**G**GTTGCATTAC**AACACTGTACCCTCCTTAT
AP-1 RUNX
AATAACACAACTATGGTTA**TGACTTA**GGCGTCG**TGTGG**AGCCTCAGTTTC

Supplemental Figure 4

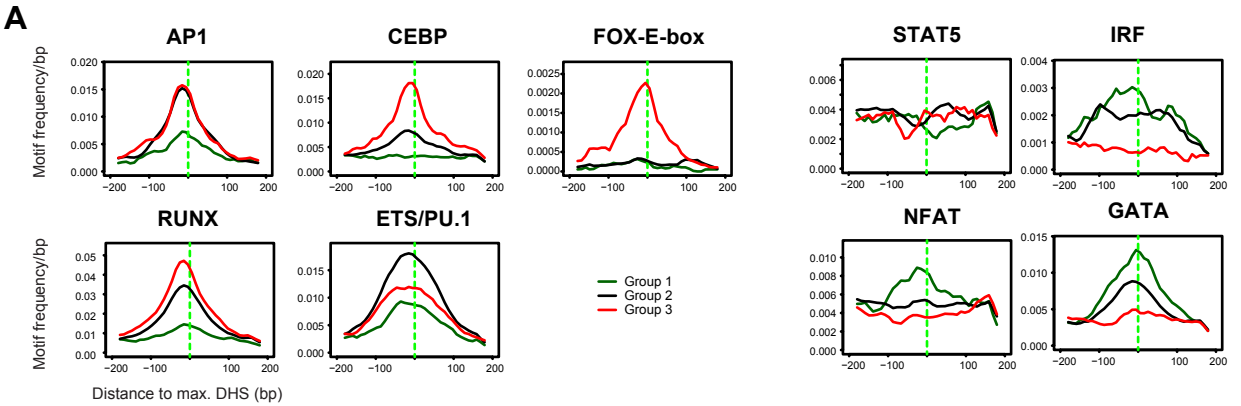

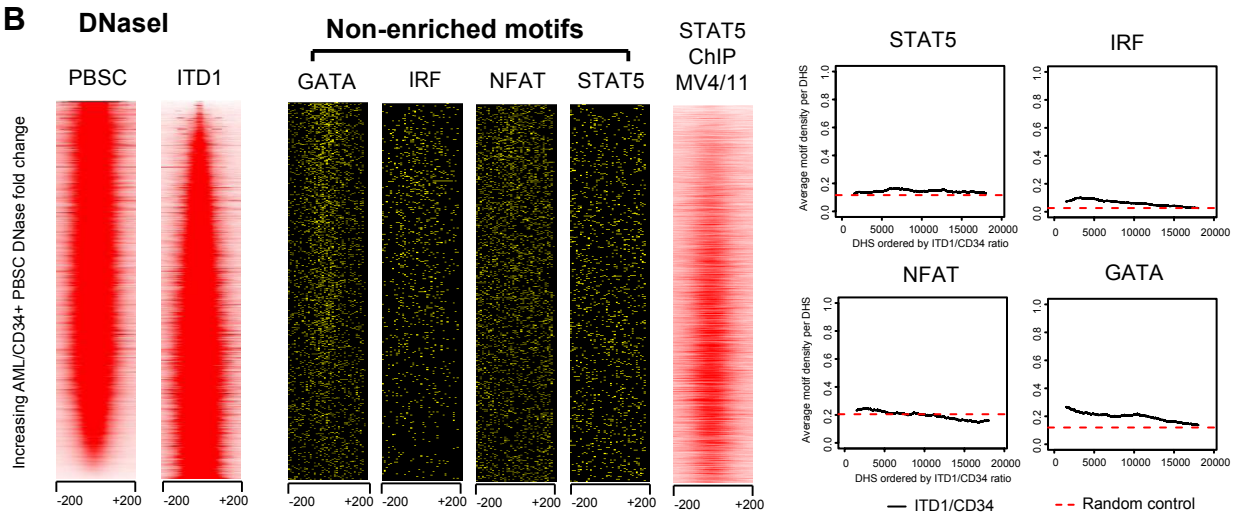

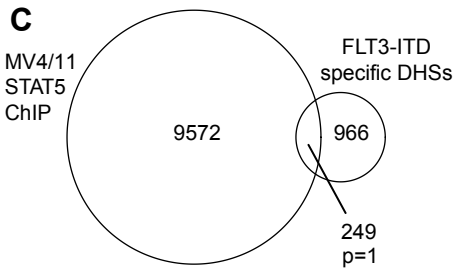

D

Motif	% targets	logo
ETS	43.7	
STAT	16.3	
RUNX	28.7	
C/EBP	19.8	
AP-1	20	

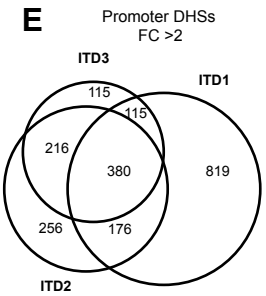

F

Motif	% targets	logo	logP
RUNX1	34.0		-37
ETS/PU.1	34.3		-30
AP-1	17.1		-22
NF-kB	8.6		-14
C/EBP	8.3		-14

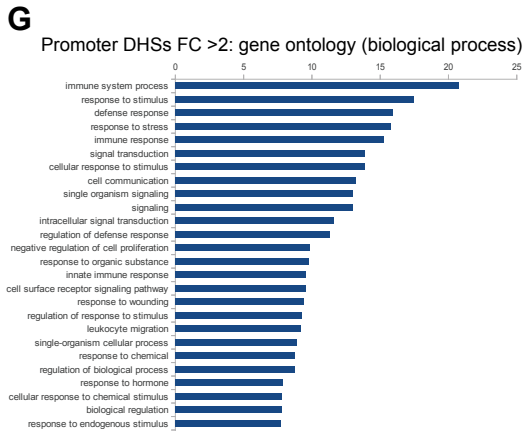

Supplementary Figure 5

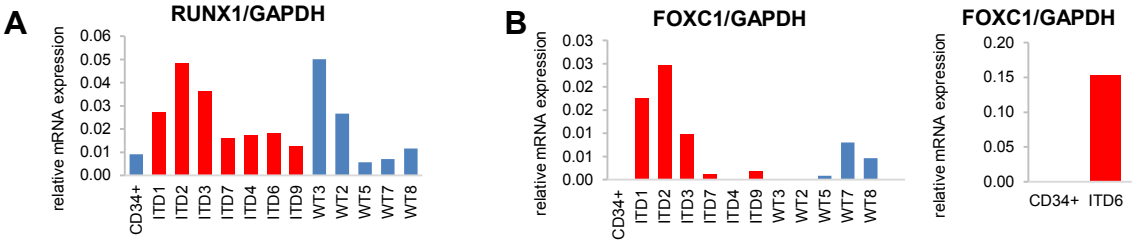

C **SCARA3 DHS**

TGCCGTCCCTCCAACTCGTCTCTAGCCAGGGCTGAGCTGACAACTTCTGT
TGCGCCAGCCCTGGATA**CACCTGTCAAAACA**GAGCCGCGGGAGAGGAGAG
CAGAGAGCTG**AAAAACA**TGGTC**TGACCACA**GTGAACTTTCCAGTGGGGCT
GGGCTAGGCTGGGCTGGCAAGCCTTGACC**TGTGGGTG**GTGTGCTGAGCAG

CTSG DHS

GTAGAAGATGGCA**TGACGTTA**TCCCCATGGCATCTCAGC**TGTGGTTT**TCC
TACTATAGCTTGCCAGCTTCT**CTGTAAAAACA**ACTCTGCCTGTCTCAGGT
ACTTCTAATGCTATTGTA**TCTTCCGGT**CATGAGGC**TGTGGTGG**GAGGACA
GTTTCCCTACAGCCTGGATGGTTGTAAAGC**TGTTTTTACT**CTGGACCCCA
CTCAAAACTGGTAGCCTTGCCGATTAC**TGAGTAA**ATGGGTAATAGGGGTA

MDGA1 DHS

CCTTCCTCCAGCCCAGCTGGTTGGATCAGGGTGGCATC**TGACTCA**AGGGC
AGCC**AACCCACA**GGTTGCCCAATGATGTATG**TGTGGCTA**GACCTGAAATG
GGGGCCTGTCCAATCAGCCCATTATCCTGAGCGGC**TGAGTCA**GTGAATGC
TGGCAGCTGCT**ACCGGAAGG**CCATGAAGGAGAGTTGAGCTGGAGAGGTCA
TGATGCCTGGAAAGCTGAAGTTA**TGAGGAAGC**AGACACCA**TGACTCA**GGA
GAGGAACTGCATGGACAAAAAGCAGCAGATGCTGGGGAGTGAC**TGAGTCA**

MED16 DHS

ACGACTTGGCTCTGGCTCTGCCGTGGCGGCACACAGG**CAGCTG**GTGCCAA
T**GAGCCACA**CTCACAAACCCAG**GCGGGGGCC**GTCAGGCCCTGGGCCGCAC
TGTGCAGACCTGAGCTATAGCACT**CAGGAAGT**GCTGTGTAAGCACCAGCG
GCTGCTGCGGGCACTATT**TGATTTCA**AATCAAATTTGTCAAGTCATTATT

GZMB DHS

TGAAGAAATGTCATAGAAAGATGAAAAATATTGAGGGAA**TGAGTTA**GGGC
TGTGAACGTACTGTGA**TTACTCA**A**TAACCACA**AACTTGCAATTAACTGCT
G**TAACCACA**AATCACCCTTCTAGGGTTCGCTGTGTAGAAAGAGCCGTTGA
TTTTTTATAGTCACTG**TAGCCACA**GCTGGAACCTCATAAAGAGTTCATGG

VSTM4/c10orf128 DHS

AGTGGCCTCTTTTCATGGGAAAGCC**CCAGGAAGT**GACGTGACCTCTTCAG
GCTCCATGCCTGAGCC**TGAGTCA**CTGGCTC**CGAGGAAGA**GTCTCACAGCA
GCATGGAGGGTGAACAGTCATTACAAACTGACCAAAGTATCTTAATGTGT
CACATG**TGACTCA**ACAATCAGGGCTCATC**TGCGGTTT**GGGAGGGTCTCTT

CCNA1 -14 kb DHS

GTTTTTCTTAACTGCTCTAT**AGATAAC**AGAAGC**ATTGTGAAAT**ATTGAGT
TTTCAATTTGAGATATGATTTCAGTTCCCCTGTACCAGTAAAACTACTAA
CAC**CAGCTG**CTCTGAAGG**ATACCACA**AAGAGC**TGACTCA**CCAAAGAATGC

D **c8orf87/FAM92A1 DHS**

GTTTG**TGTTTACACAGGTGTGGCCA**TATTTAACAAAAAAATTTTTTATGC
ACTA**TGCAAACA**GCTGCCTGTC**TGTTTTTCT**TTGGCAGAGTTCTTTCCAAC
TGAAACAACTTATATCAAGCACATCGCTCTGTGATACTTA**TATAAACA**AC
ACAGAAA**AATTCCTG**TAC**AAGGAAGA**GGTTTCTCATAATGTGTCTGACAG

Supplemental Figure S6

A Footprints in ITD-specific DHSs

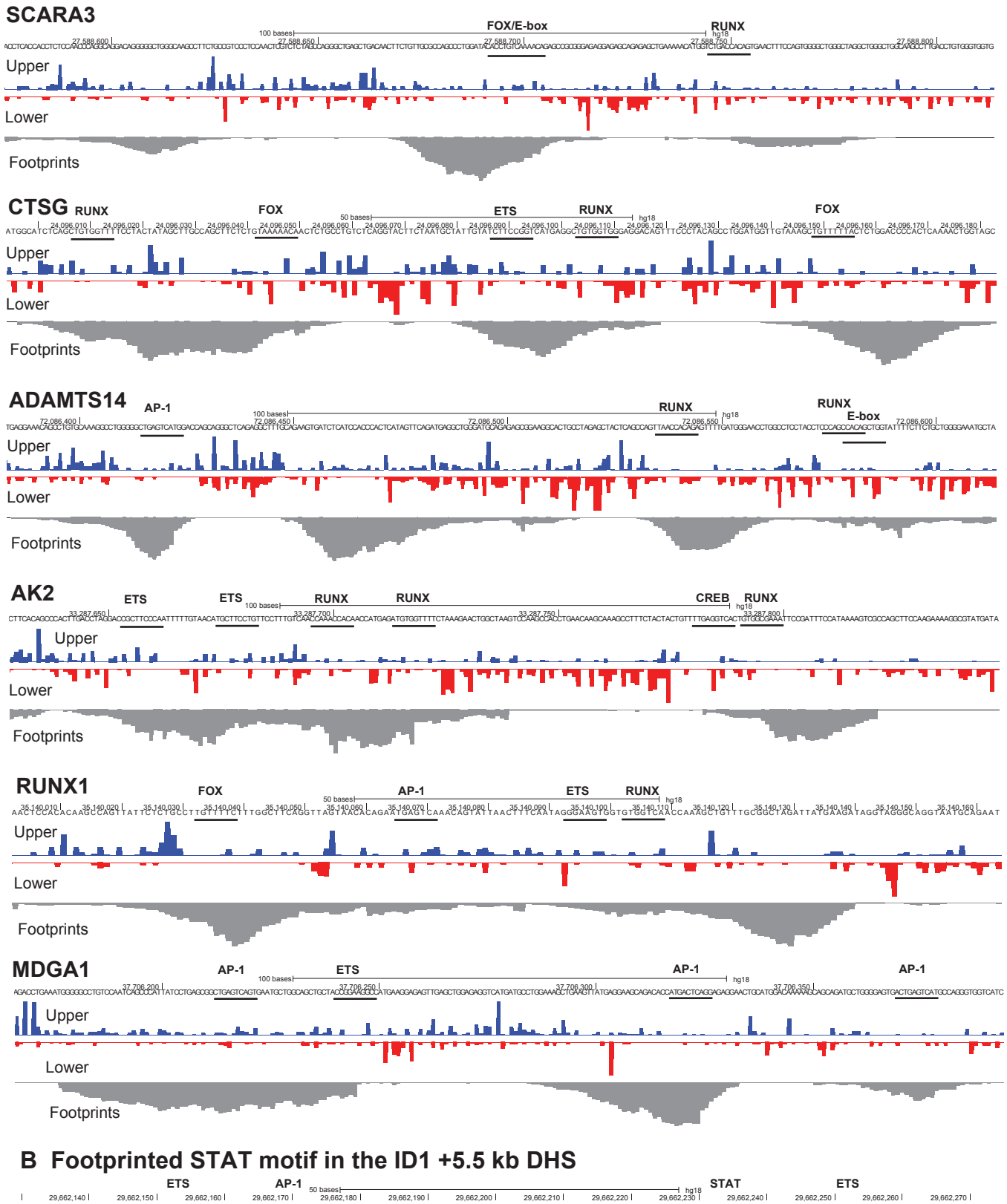

B Footprinted STAT motif in the ID1 +5.5 kb DHS

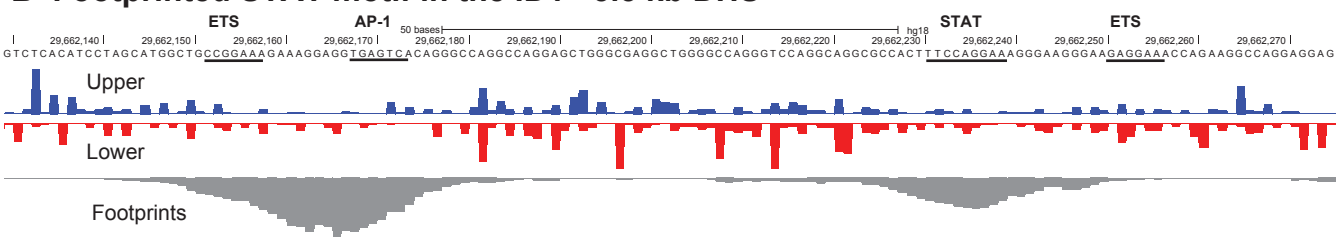

Supplemental table, figure, and data file legends

Table S1. Related to Figure 1.

List of genes and exons screened for mutations, including the total number of independent mutations found for each gene.

Figure S1. Related to main figure 1.

FLT3-ITD+ AML displays a characteristic mRNA expression profile.

(A) Log2 mRNA microarray values for 7 FLT3-ITD+ AML-specific target genes, plus *TBP* which serves as a control. Values are shown for the samples listed in **Table 1**, as well as for the average of 3 independent PBSC microarray analyses, the average of a central core of 3 ITD+ AML samples (ITD1, ITD2 and ITD3), the average of 4 additional ITD+ AML samples (ITD4, ITD6, ITD7 and ITD8), and the average of a core of 4 WT FLT3 AML samples (WT2, WT3, WT5 and WT7). Patients carrying RUNX1 mutations are labeled R, and patients with mutations in the signaling proteins NRAS or SOCS1 plus PTPN11 are labeled with an asterisk. **(B and C)** Expression of all annotated FOX genes **(B)** and 10 down-regulated MHC class II genes **(C)** in ITD+ AML (blue) and WT FLT3 AML (red) relative to PBSCs. Values shown represent the change in the average log2 values for the core group of 3 ITD+ AMLs (ITD1, ITD2 and ITD3) and for the core group of 4 WT FLT3 AMLs (WT2, WT3, WT5 and WT7) relative to the average log2 values for 3 PBSC data sets.

Figure S2. Related to main figure 3.

FLT3-ITD+ AML has a characteristic chromatin signature.

(A and B) Profiles of the DNase-Seq signals within each 400 bp window centered on each distal DHS peak for ITD2 compared to PBSCs **(A)** and ITD3 compared to PBSCs **(B)**, with peaks shown in the order of increasing DNase-Seq tag count signal for ITD2 or ITD3 relative to PBSCs. In each case these analyses include the union of all distal peaks present in either the AML sample or in PBSCs. Shown to the right of the DNase-Seq profiles are the relative mRNA expression values for genes with the nearest transcription start sites (TSS) in ITD2 or ITD3 relative to PBSCs, and the DNA methylation signals for the DHSs in ITD2 relative to PBSCs.

(C) Profiles of the DNase-Seq signals within each 400 bp window centered on each promoter-associated DHS peak for ITD1, ITD2 and ITD3 compared to PBSCs, with peaks shown in the order of increasing DNase-Seq tag count signal for the AML sample relative to PBSCs.

(D) Rolling averages of the DNase-Seq tag counts, plus the AML/PBSC ratios of these values for the DHSs depicted in **Figures 2E**, **S2A** and **S2B**.

(E) Side-by-side comparison of all the distal DHSs present in the ITD1/PBSC data set, ranked in order of increasing relative DNase-sensitivity as in **Figure 2E**, plus the DNase-Seq profiles across the same regions for the other samples depicted.
(F) Average DNase-Seq profiles across each of 3 groups of DHSs, grouped as indicated to the left, separated on the basis of a 2-fold difference between PBSCs and ITD1.

Figure S3. Related to main figure 4.

FLT3-ITD mutations are associated with a specific subset of DHSs.
(A and B) UCSC Genome browser views for DNase-Seq and RUNX1 ChIP-Seq data for ITD-specific DHSs (marked by red ovals) located near ITD-specific genes. Shown underneath these data are the profiles for a STAT5 ChIP assay of MV4-11 cells. ITD-specific DHSs are enclosed by red ovals. The log2 mRNA microarray values for some of the ITD-specific genes, displayed as in **Figures S1A** and **3F**, are shown in panel **B**. The mRNA values for *FOXC1*, *DSC2* and *HOXB4* are shown in **Figure S1A**. Note that the *C10orf128* locus is also a member of the group of 134 ITD-specific mRNAs, and that *ID1* is a known FLT3-ITD target gene (Tam et al., 2008) but is not ITD+ AML-specific. The DNA sequences are shown for 4 of the highlighted DHSs, with the regulatory motifs underlined in bold.

Figure S4. Related to main figure 5.

ITD-specific DHSs have a specific motif signature.
(A) Average densities of motifs across each of the 3 groups of distal DHSs subdivided as indicated at the left of **Figures 2E** and **4B** on the basis of relative DNase sensitivity.
(B) Alignment of STAT5, IRF, NFAT and GATA motifs with distal DHSs present in either ITD1 or PBSCs with the rolling averages of motif densities plotted on the right. Data is depicted in the same fashion as in **Figure 5B**, and with the MV4-11 STAT5 ChIP data presented alongside on the same coordinates.
(C) Venn diagram depicting the overlap between the MV4-11 STAT5 ChIP peaks and the 1216 ITD-specific DHSs.
(D) Motifs identified using HOMER to analyze the MV4-11 STAT5 Chip peaks.
(E) Venn diagram depicting the overlap between populations of promoter-associated DHSs that are 2-fold upregulated in AML samples ITD1, ITD2 and ITD3 compared to PBSCs (FC>2).
(F) Result of de novo motif search of 380 ITD-specific promoter-associated DHSs using HOMER.
(G) Gene ontology analysis of genes with ITD-specific promoter-associated DHSs.

Figure S5. Related to main figure 6.

FOXC1 and RUNX pathways are activated in ITD+ AML.

(A and B) Quantitative PCR/reverse transcriptase analysis of *RUNX1* **(A)** and *FOXC1* **(B)** mRNA levels in a subset of the AML samples listed in **Table 1**, and in CD34+ PBSCs. Values are expressed as mRNA levels relative to GAPDH mRNA.

(C and D) DNA sequences of ITD-specific DHSs associated within the *SCARA3, CTSG, MDGA1* and *c8orf87/FAM92A1, MED16, GZMB, c10orf128, and CCNA1* loci. Motifs representing the ITD-specific DHS signature are underlined in bold. The log2 mRNA microarray values for *FAM92A1* in panel D are displayed as in **Figure S1**.

Figure S6: Related to main figure 7.

ITD-specific DHS motifs are occupied in ITD+ AML.

(A and B) DNase I cleavage patterns spanning representative ITD1-specific footprints predicted by Wellington. Upper strand cut site frequencies are shown in blue and lower strand cut site frequencies are shown in red for ITD1. The relative probabilities for the presence of footprints predicted by Wellington are indicated by the grey histograms. ITD-specific DHS signature motifs that exist within predicted footprints are underlined in bold. Panel B displays a DHS that is 5 kb downstream of *ID1* that encompasses a footprinted STAT motif.

Supplemental data file 1. Related to Figure 1.

List of all the individual gene mutations identified from the mutation screen, including the DNA and amino acid changes, the proportion of sequences mutated (allele bias), the number of wild type and mutated sequences detected (allele depth), the method used for the mutation detection (Pindel or GATK), the nature of the 2 alleles (0=normal, 1= mutated), the lengths of insertions (INS) and deletions (DEL), and whether the mutation is previously recorded in the COSMIC database.

Supplemental data file 2. Related to Figure 1.

Alphabetical list of 134 upregulated genes and 77 downregulated genes in FLT3-ITD+ AML. Data is based on values obtained in **Figure 1** for the relative differences in the average log2 mRNA array values for the core group of ITD+ AML samples (ITD1, ITD2 and ITD3) relative to the other four populations defined in **Figure 1**. Also listed are the actual average log2 mRNA array values for each of the five populations.

Supplemental data file 3. Related to Figure 4.

Chromosomal coordinates of 1216 FLT-ITD+ AML-specific DHSs in the hg18 build of the human genome sequence. DHSs are listed alphabetically according the name of the nearest gene, and indicating the distance to the nearest transcription start site (TSS).

SUPPLEMENTAL EXPERIMENTAL PROCEDURES.

Patient sample, PBSC and CD14+ cell processing

Essentially all of the samples included in the collection described in Supplementary data File 1 are diagnostic samples from presentation cases before treatment. The two exceptions are a control sample with a JAK2 mutation from a patient who had progressed from MPD to AML, and sample ITD8 which came from a relapse of AML. All human tissue was obtained with the required ethical approval from the NHS National Research Ethics Committee. Most of the samples used in this study were surplus diagnostic samples obtained from the Haematological Malignancy Diagnostic Service (St James's Hospital, Leeds, UK), where cytogenetic abnormalities and sample immunophenotype were also determined at the time of disease diagnosis. Additional AML samples were obtained from the Centre for Clinical Haematology, Queen Elizabeth Hospital Birmingham, Birmingham, UK, and the West Midlands Regional Genetics Laboratory, Birmingham Women's NHS Foundation Trust, Birmingham, UK. AML samples were processed on the same day that they were received. Mobilized PBSCs were provided by NHS BT, Leeds, and NHS BT, Birmingham, in the UK.

For all samples used in this study, mononuclear cells were purified from bone marrow (BM), peripheral blood, or mobilized peripheral blood stem cells from patients or donors by differential centrifugation (20 mins, 2300RPM/881g, acceleration:4, no brake) using Lymphoprep (Axis-Shield UK, Cambridgeshire, UK). For most samples, undifferentiated blast cells were then isolated using antibody-coupled MACS Micro Beads (Miltenyi Biotec) and separation on magnetic columns (Miltenyi Biotec) according to the manufacturer's guidelines, using CD34 antibodies in most cases, and CD117 antibodies in 3 cases. For 6 samples with greater than 92 % blast cells (before the purification of mononuclear cells) the column purification was not performed. PBSCs were purified as for CD34+ AML cells, and CD14+ BM cells were obtained from orthopedic patients and were purified by the same protocol but using CD14 antibodies.

Cell lines

The cell lines MOLM14, MV4-11, THP1 and U937 were cultured in an incubator at 37^0C in GIBCO™ 1640 RPMI + Glutamax™ medium supplemented with 10% heat inactivated fetal calf serum (GIBCO), 100 U/ml Penicillin, 100 mg/ml Streptomycin.

DNAse-Seq library preparation

DNase-Seq libraries were prepared essentially as previously described (Ptasinska et al., 2014). To perform this global mapping of DHSs, DNase I digestions of permeabilized cells were performed as previously described (Bert et al., 2007). In this procedure, live cells were added directly to a solution of DNase I in dilute NP40, digested for 3 min at 22ºC, and the reactions then terminated by addition of SDS to 0.5%. This protocol maximizes the likelihood that transcription factors will remain bound during the digestion period, thereby increasing the probability of detecting DNase I footprints. DNase I (DPFF) was obtained from Worthington Biochemical Corporation and typically used in the range of 2-6 µg/ml using a final 1.5 x 10^7 cells/ml. The DNA digestion extent was comparable in all the generated samples as measured by RT-PCR (Ptasinska et al., 2012). The resulting cell lysates were then treated with 0.5 mg/ml Proteinase K overnight at 37 °C, then in 0.2 mg/ml RNAse A for 1 hour at 37ºC. DNA was isolated by phenol/chloroform extraction. Levels of DNase I digestion were assessed using quantitative real-time PCR, measuring the ratio of the presence of known DNase I hypersensitive regions compared to a more resistant inactive region. Sequences of the PCR primers used for this purpose were, for the active region, *TBP* promoter 5´-CTGGCGGAAGTGACATTATCAA and 5´- GCCAGCGGAAGCGAAGTTA; and for the inactive region, a region of chromosome 18: 5´- ACTCCCCTTTCATGCTTCTG and 5´-AGGTCCCAGGACATATCCATT. DNase-Seq samples were generated from a size selection of DNase I-digested DNA fragments comprised within a range of 100 to 250 bp (not including linkers) and subjected to library preparation as per manufacturer´s instruction (Illumina). Libraries were run on Illumina GAIIx, HiSeq 2000 and 2500 sequencers.

Chromatin immunoprecipitation

ChIP-Seq assays were performed essentially as previously described (Ptasinska et al., 2014). In this procedure, cells were resuspended in 10 ml of growing medium, and cross-linked with 1% formaldehyde (equivalent to ~0.33 M) for 10 min at RT. The cross-linking reaction was stopped by adding glycine in excess of the formaldehyde to a final concentration of 0.4 M, followed by two washes with ice–cold PBS. Cells were resuspended in 10 ml of ice-cold ChIP buffer A (10 mM HEPES pH 8.0, 10 mM EDTA, 0.5 mM EGTA, 0.25% Triton X-100, proteinase inhibitor cocktail (Roche UK, Burgess Hill, UK) and 0.1 mM PMSF), incubated for 10 min at 4°C with rotation, and centrifuged 5 min at 500 x g at 4 °C. The pellet was resuspended in 10 ml of ice–cold ChIP buffer B (10 mM HEPES pH 8.0, 200 mM NaCl, 1 mM EDTA, 0.5 mM

EGTA, 0.01% Triton X-100, protease inhibitor cocktail and 0.1 mM PMSF), incubated for 10 min at 4 °C with rotation and centrifuged for 5 min at 500 x g at 4 °C. Cells were resuspended in 600 µl of ice-cold ChIP lysis buffer (25 mM Tris-HCl pH 8.0, 150 mM NaCl, 2 mM EDTA, 1% Triton X-100, 0.25% SDS, protease inhibitor cocktail and 0.1 mM PMSF), incubated 10 min on ice and sonicated at 5 °C using a Bioruptor™ (Diagenode, Liege, Belgium) to generate fragments an average length of 400-500 bp (10 min with 30 s "ON" and "OFF" cycles, power setting high). The lysates were centrifuged for 5 min at 16,000 x g at 4 °C and the supernatants were diluted with two volumes of ice-cold ChIP dilution buffer (25 mM Tris-HCl pH 8.0, 150 mM NaCl, 2 mM EDTA, 1% Triton X-100, 7.5% glycerol, protease inhibitor cocktail and 0.1 mM PMSF). For each IP, 15 µl of Dynabeads® protein G were pre–incubated with 50 µg BSA and 2 µg antibody against RUNX1 (Abcam, ab23980) for 2 h at 4 °C with rotation. The blocked antibody-bound protein G mix was added to 20–25 µg chromatin in a total volume of 500 µl diluted ChIP lysis buffer and incubated for 2 h at 4°C with rotation. After magnetic separation the beads were washed once with 1 ml wash buffer 1 (20 mM Tris-HCl pH 8.0, 150 mM NaCl, 2 mM EDTA, 1% Triton X-100, 0.1% SDS), twice with 1 ml wash buffer 2 (20 mM Tris-HCl pH 8.0, 500 mM NaCl, 2 mM EDTA, 1% Triton X-100, 0.1% SDS), once with 1 ml LiCl buffer (10 mM Tris-HCl pH 8.0, 250 mM LiCl, 1 mM EDTA, 0.5% NP-40, 0.5% Na-deoxycholate) and twice with 1 ml TE/NaCl buffer (10 mM Tris-HCl pH 8.0, 50 mM NaCl, 1 mM EDTA). For each wash the beads were mixed with ice-cold washing buffers for 10 min at 4 °C. The immunoprecipitated DNA was eluted two times with 50 µl ChIP elution buffer (100 mM NaHCO3, 1% SDS) for 15 min at RT with shaking. At this step the input control (1% of the starting material) was included in the experimental procedure after first adjusting the final volume to 100 µl with ChIP elution buffer. The eluted DNA was incubated overnight at 65 °C in the presence of 50 µg proteinase K. The DNA was finally purified using Agencourt AMPure (Beckman Coulter) magnetic beads according to the manufacturer's instructions, eluted with 50 µl x TE.

ChIP assays of MV4-11 cells with control 2 µg of IgG (Millipore 12-370), 2 µg of Runx1 (Abcam, ab23980/GR2016781) 2 µg of STAT5 (Santa Cruz SC-835) and 5 µg of cFos (Santa Cruz SC-253) antibodies were performed by a modification of the above procedure, using 2 cross-linking agents. Cells were first washed with PBS and then cross-linked with Di(N-succinimidyl) glutarate (DSG) (Sigma, 8424-500MG-F). For each assay, 2 x10^7 cells were suspended in 30 mls PBS and incubated with 250 µl DSG (50mg/500µlDMSO) on a rotating wheel for 45 minutes at room temperature. After 45 minutes cells were washed 4 times with PBS and suspended in 10 mls of PBS. Cells were then cross-linked for a second time with 1% Formaldehyde for 10 minutes at room temperature. Cross-linking was terminated by adding 4 volumes of cold PBS+0.125 M of Glycine. Cells were washed with cold PBS, lysed and

sonicated (15 min with 30 s “ON” and “OFF” cycles, power setting high) and finally used for Chromatin Immunoprecipitation assays as above.

The quantitative PCR primers used for Fos and Runx1 ChIP assays had the following sequences.
MDGA1 DHS: GGGTGGCATCTGACTCAAG and ACTCTCCTTCATGGCCTTCC.
C10orf128 DHS1: CAAGGGCCTCTCTTGGGG and GACTGTTCACCCTCCATGCT.
CCNA1 (-14) DHS: ACTACTAACACCAGCTGCTCT and TGGTTAGGGTAAGGGGCATG.
GZMB DHS: GGAATGAGTTAGGGCTGTGAA and TCTTTATGAGGTTCCAGCTGTG.
CSF1R-FIRE DHS: GCCTGACGCCAACAATGTG and GGCAAAGGAGGGAAGTGAGAG.
IVL promoter: GCCGTGCTTTGGAGTTCTTA and CCTCTGCTGCTGCCACTT.

Mutation detection

Targeted exon sequencing of 55 cancer-associated genes was performed by the West Midlands Regional Genetics Laboratory using 1212 pairs of PCR primers, as summarized in **Supplemental Table 1** for amplification using a RainDance Technologies platform. The mutation sequence data summarized in Supplemental Data File 1 was analyzed using algorithms to detect either (i) nucleotide variants using the Genome Analysis Toolkit (GATK) (DePristo et al., 2011) or insertions and deletions using Pindel (Ye et al., 2009). Mutations were also screened against the COSMIC data base of previously observed mutations (http://cancer.sanger.ac.uk/cosmic/).

FLT3-ITD detection PCR

FLT3-ITD detection on genomic DNA from patient samples was adapted from a technique used to detect FLT3-ITD variants on cDNA (Kelly et al., 2002) using Taq polymerase (Life Technologies). Primers used to detect a wild-type amplicon size of 394 bp were:
FLT3det-FW: GGTGTTTGTCTCCTCTTCATTGT
FLT3det-RV AAAGCACCTGATCCTAGTACCTT
PCR products were separated on a 1.5% agarose gel.

EMSAs

Electrophoretic mobility shift assays were performed using an AP-1 probe as described previously (Cockerill et al., 1993).

Western blotting

Cells were lysed in RIPA buffer (Cell Signalling). After electrophoresis of protein extracts on polyacrylamide gels, proteins were transferred to nitrocellulose membranes (Thermo

scientific, Pierce) using a Mini-Trans blot cell (Bio-Rad). The membranes were blocked with 5% (w/v) milk powder in TBS-Tween 20 (0.1%) (TBST) at RT for 1 h and then incubated overnight at 4 °C with primary antibodies. Incubation with an anti-rabbit IgG, HRP-linked secondary antibody (TrueBlot, Rockland 18-8816-33) followed at RT for 1 h. Membranes were developed using the ECL Plus Western Blotting detection system (GE Healthcare) according to the manufacturer's protocol and signal was detected using autoradiography .
The antibodies used were supplied by Cell Signalling, with catalog numbers, as follows: FLT3 3462, Erk1/2 9102, Phospho Erk1/2 9101, Stat5 9363, Phospho Stat5 9359,
RSK2 9340, Phospho RSK2 3556, GAPDH 2118.

siRNA treatment in MV4-11 cells

$10x10^6$ MV4-11 cells were transfected with 300 nM of the control siRNA MMsiRNA (QIAGEN 1027286) and 300 nM of FLT3 siRNA with modification 5'-Cy5 (QIAGEN SI00059871) by using the Amaxa Cell Line Nucleofector kit L (VCA-1005). Cells were incubated in RPMI medium for 24 hours at 37°C. After this incubation time cells were washed with PBS and the efficiency of transfection was verified by FACs analysis. Then 1 $x10^6$ cells were used for RNA extraction (gene expression analysis), 2 $x10^6$ cells were used for protein extraction (Western blot) and the remaining of cells were used for Chromatin Immunoprecipitation assays.

The siRNA directed against FLT3 has the following sequences:
Sense strand: 5'-GGUUUAAAGCCUACCCACATT-3'
Antisense strand: 5'-UGUGGGUAGGCUUUAAACCTG -3'

MAPK inhibitors treatment in MV4-11 cells

$20x10^6$ MV4-11 cells were treated with 25 μM of 50 μM of PD98059 (Cell signalling No 9900) , SP600125 (Cell signalling No 8177) and 25 μM of SB202190 (Cell signalling No 8158) inhibitors, directed against MEK1/2, JNK and p38 respectively. Cells were incubated with DMSO (control) and inhibitors in RPMI medium for 5 hours at 37°C. After this incubation time cells were washed with 1X PBS and $1x10^6$ cells were used for RNA extraction (gene expression analysis)), $2x10^6$ cells were used for protein extraction (Western blot) and the remaining of cells were used for Chromatin Immunoprecipitation assays.

Gene expression microarray analysis

1-2 μg RNA was isolated from patient and donor samples via Trizol™ extraction. Sizes and quality of RNA preparations were checked using a RNA 6000 Pico Chip with a Bioanalyzer 2100 system (Agilent). 100 ng RNA was labelled with Cyanine 3-CTP according to the sample preparation protocol from Agilent: One-Color Microarray-Based Gene Expression Analysis (Low Input Quick Amp Labeling). Amplified labelled RNA samples were purified by using

Qiagen's RNeasy mini spin columns and cRNA quantified by using a Nanodrop spectrophotometer. Hybridisation samples were prepared for a 8-pack microarray using 600 ng cRNA each according to the hybridisation protocol from Agilent: One-Color Microarray-Based Gene Expression Analysis (Low Input Quick Amp Labeling), loaded onto as 8-pack SurePrint G3 Human GE 8x60K Microarray kit v1 design ID 028004 (Agilent) and hybridized at 65 °C overnight. After washing, microarrays were scanned on an Agilent G2565C Microarray Scanner using the Profile AgilentG3_GX_1Color for 8x60K microarrays (Dye channel: Green; Scan region: Scan Area (61 x 21.6 mm); Scan resolution (µm): 3; Tiff: 20 bit). Probe signals were extracted via the Agilent Feature Extraction software (version 10.7.1.1), protocol GE1_107_Sep09, using grid number 028004_D_F_20110325 (SurePrint G3 Human GE 8x60K). Arrays were normalized via quantile normalization in *R* using the *limma* package (Smyth et al., 2005). Transcript annotations were aggregated into unique gene names, whereby the mean of transcripts was computed for genes with more than one transcript. Genes with log2 intensities greater than 6.5 were considered expressed. Genes were considered enriched over CD34+ PBSC, WT AML and CD14+ PBSC using a two-fold change cutoff. The Pearson correlation matrix for all samples was computed in *R* and subsequently clustered via hierarchical clustering using *cluster 3.0* (de Hoon et al., 2004), with row, column Pearson correlation clustering and complete linkage. Heatmap images were generated via *Java TreeView* (Saldanha, 2004). For AML/ PBSC fold mRNA signal change heatmaps, expression fold change values were retrieved for each DHS, using values of the closest gene. Fold change values were sorted by increasing AML/ PBSC DHS fold change and plotted as heatmaps using *Java TreeView*.

Gene expression analysis by reverse transcriptase quantitative PCR analysis.

Gene expression patterns were confirmed by Real Time PCR analysis as previously described (Ptasinska et al., 2014). The PCR primers used were as follows:

GAPDH: CCTGGCCAAGGTCATCCAT and AGGGGCCATCCACAGTCTT.

FAM92A1: GGATGCTAGCCGAACAAGTC and ACCTCTAAAGCTTTGCCGTG.

CTSG: TCCTGGTGCGAGAAGACTTTG and GGTGTTTTCCCGTCTCTGGA.

NOV: CACGGCGGTAGAGGGAGATA and GGGTAAGGCCTCCCAGTGAA.

CCNA1: AGCACTTTTGGCCAGAAACC and GCTGAGGTCGATGGGGTATA.

PRTN3: CTCAATGTCACCGTGGTCAC and GGCCACCTGAGTCTCCGAA.

PT4A3: (PRL3): GCTTCCTCATCACCCACAAC and CGGCGTTTTGTCATAGGTCA.

IL2RA: CTGCCACTCGGAACACAAC and CTCGCTTGGTCCACTGGC.

FOXC1: CCCTCTCTTGCCTTCTTCCT and CGTCAGGTTTTGGGAACACT.

RUNX1: As used previously (Ptasinska et al., 2014).

DNA methylation array analysis

DNA methylation analysis was performed by Gen-Probe (UK) using an Illumina 450K methylation array kit. Methylation intensities were obtained via Illumina GenomeStudio to process array image files, probeset extraction and normalization. Per promoter intensities were retrieved via the *IMA R* package (https://www.rforge.net/IMA/index.html). Genome-wide coverage files (where probe data was available) were obtained using custom *R* and *Perl* scripts by generating *BED* files corresponding to intensities for all probes, followed by *WIG* format conversion.

Bioinformatic analyses

High-throughput sequencing alignment, peak detection and filtering

Sequencing reads were obtained as *FASTQ* files and uniquely aligned to the hg18 genome with *bowtie* using the following parameters: *--all --best --strata -v 2 -m 1*. For reads obtained from the HiSeq2500 sequencing platform, reads were retrieved in *BCL* format, converted to *FASTQ* via *bcl2fastq* and subsequently aligned using the same parameters. For samples run on more than one lane, the resulting *FASTQ* files were used as multiple inputs in *bowtie*, resulting in separate lanes being aligned together. Total and aligned read statistics are as follows:

Patient	total reads	aligned reads	peaks
PBSC	193,127,800	167,785,230	31,577
CD14+ BM	17,876,715	11,277,407	16,268
ITD1	496,164,295	342,121,088	25,156
ITD2	563,648,832	491,149,277	24,362
ITD3	31,191,334	22,512,783	27,899
ITD4	45,626,146	35,117,991	30,124
ITD5	232,690,946	172,049,755	26,127
WT1	173,684,899	155,121,178	25,091
WT2	46,523,235	34,921,707	23,592
WT3	27,668,387	22,368,270	26,510
WT4	33,683,955	28,775,417	20,707
WT5	38,565,964	33,615,251	25,868
WT8	56,390,352	40,690,809	37,406

To generate DHS coverage tracks, aligned reads were processed using a previously described bioinformatics pipeline (Koch et al., 2011). Briefly, fragment size was estimated using iterative extension, whereby the maximum overlap of reads corresponded to the mean

fragment size. Bases showing more than 5 read starts were considered as clonal artifacts and discarded. Reads were subsequently extended to the estimated size and depth coverage was derived by counting the number of reads in 10-bp windows genome-wide as fixed-length *WIG* files. Peak detection was subsequently carried out using *CoCAS* following *WIG* to *GFF* conversion. Peak detection parameters were set to the signal mean + 2 standard deviation ($p \leq 0.05$) for the both peak and extension thresholds. To account for further sequencing and/or repeat artifacts, peaks were cross-checked against an hg18-converted version of the ENCODE blacklist (ENCODE Project Consortium, 2012) via *bedtools* (Quinlan and Hall, 2010). Intersecting peaks were discarded as artifacts. Total numbers of peaks are indicated above.

Generation of peak summit unions

For AML vs CD34+ PBSC DHS comparisons, peak summit unions were performed as previously described (Kreher et al., 2014). Essentially, peaks were annotated to the nearest isoform for which a distance criterion of 5 kb upstream or downstream of the TSS was used to treat peaks as distal or proximal. Distal and proximal peaks were subsequently treated separately. Unions were computed as the concatenation of AML and CD34+ PBSC datasets, with peak summits closer than 400 bp being treated as one same peak. In this case, the average peak summit coordinate was used as the merge of both. DHS coverages were retrieved [-200bp; +200bp] around the union summits using custom Perl scripts. Distributions of coverages were plotted and tested positive for normality via Shapiro-Wilkes normality tests in *R*. Coverages were consequently normalized via log2 transformation, centre-scaling to the AML dataset and ranked by log2 AML/CD34+ PBSC fold change to account for read depth heterogeneity. To minimize redundancy, further overlaps of merged and other union summits (left as they were during the merging process) within 400 bp resulted in the first one in genomic coordinate order being retained. To avoid error values, values of 0 tags were replaced by 1 prior to log2 transformation. Heatmap images were generated via *Java TreeView*. Average signal profiles by increasing DHS fold change were computed using a rolling average with a window size of 1500.

DHS clustering

For total DHS clustering, the union of all distal, primary AML (FLT3-ITD, WT) and CD34+ PBSC DHS summits was computed. Tag coverages were recovered [-200 bp to +200bp] around the union of all summits, log2 transformed, center-scaled and expressed as log2 AML/CD34 fold change, with log2 signal intensities of 0 changed to 1. All values were collated into a single table. Hierarchical clustering was performed via *cluster 3.0*, using Pearson correlation clustering for row and column clustering, as well as single linkage due to the table size. For DHS correlation clustering, tags were recovered, log2 transformed and normalized

following the exact same procedure. A correlation matrix for all samples was computed in *R* and subsequently clustered hierarchically via *cluster 3.0*, using Pearson correlation clustering for rows and arrows, as well as complete linkage. Heatmap images were generated via *Java TreeView*.

Intersection of AML and CD34+ PBSC enriched DHSs, DHS group definition and average profiles

To define groups of DHSs with regards to their enrichment status vs CD34+ PBSC, we computed intersections of three representative FLT3-ITD AML/CD34+ PBSC unions (ITD1, ITD2 and ITD3) and selected DHSs that had a two-fold higher AML/PBSC signal ratio. Since for each union, the AML/CD34+ PBSC DHS fold change followed a normal distribution, we used the same two-fold threshold as the cutoff for AML/PBSC under-enrichment. All DHSs in between -1 and 1 log2 fold change were considered as shared between AMLs and CD34+ PBSCs. Per group average profiles for DNase I, ChIP-Seq, motif frequencies, CpG methylation were generated via a previously described *R* pipeline (Fenouil et al., 2012). Microarray gene expression and CpG methylation fold change boxplots were generated using *R*.

Significance of overlaps

2-way intersection p-values were computed in *R* using hypergeometric tests in the *ChIPpeakAnno* package (Zhu et al., 2010). 3-way intersection p-values were by deriving the distribution of probabilities for intersections of random samples with sizes corresponding to actual samples, via bootstrapping (10,000 iterations). The actual intersection p-value was retrieved by obtaining the p-value corresponding to the overlap in the simulated distribution of probabilities.

Motif discovery and heatmap generation

Motif discovery was performed via the *findMotifsGenome* function of *Homer* (Heinz et al., 2010) with a window of -200 bp to +200 bp around the summit. Solely de novo motif enrichment was considered to minimize motif redundancy. For composite motifs, motif length optimization was performed for full-length identification. Motif heatmaps were derived via the *annotatePeaks* function of *Homer* using all enriched motifs simultaneously, followed by custom *Perl* scripts to separate motif outputs. Individual motif presence tables were generated for 200 bp upstream and downstream of each summit for every consequtive10 bp windows and sorted by AML/ PBSC DHS fold change. Random occurrences of motifs were computed by performing motif discovery in similarly sized random sets of coordinates.

Motif co-occurrence clustering analysis

Motif co-occurrence clustering was essentially performed as previously described (Ptasinska et al., 2014). Briefly, digital genomic footprinting outputs from AML and CD34+ PBSC DHS samples were intersected and defined as AML-specific, shared or CD34+ PBSC –specific via the *bedtools intersect* function. Specific populations were scanned using motif matrices from *Homer*, via the *annotatePeaks* function of *Homer*. Motif mapping outputs were converted to the *BED* format. To obtain motif co-occurrence, motifs containing footprints were all intersected using the intersection_matrix function of the pybedtools package (Dale et al., 2011). We restricted motif selections to those corresponding to TFs that were actually expressed in any of our analyzed cell types. To assess significance with regards to random occurrence in footprints, we sought to estimate over-representation of occurrence as compared to background co-occurrence all footprints. We thus chose the union of AML plus CD34+ PBSC footprints. Background co-occurrence was estimated using bootstrapping (1000 repetitions) of motif mapping and co-association counts (within 50 bp) in randomly selected footprints within the background, using equally sized populations as the original number of specific footprints. Motif mapping was carried out via the *annotatePeaks* function of *Homer*, non-redundant, non-composite matrices

Corresponding ChIP-Seq heatmaps

ChIP-Seq tag counts were recovered for 200 bp upstream and downstream of merged DHS union summits via custom Perl scripts. Rows were reordered accordingly for each DHS union. Heatmap images were generated via *Java TreeView*. Average profiles by increasing AML/ PBSC DHS signal ratio were computed in *R* using a moving average with a window size of 1500.

Digital genomic footprinting

High-depth DHS datasets (ITD1, ITD2, and CD34+ PBSC) were aligned as described and subsequently converted to the sorted BAM format, whereby an index was generated via *samtools* (Li et al., 2009). DHSs were specifically identified using the *findPeaks* function of Homer. Digital genomic footprinting was performed using the *Wellington_footprints* function of the *Wellington* algorithm (Piper et al., 2013) on AML and CD34+ PBSC DHSs. DHS cut coverages, strand imbalance heatmaps and average profiles were generated using the *dnase_wig_tracks*, *dnase_to_javatreeview* and *dnase_average_profile* functions of Wellington. AML-specific footprints were identified by computing differences in footprinting occupancy scores at given genomic coordinates for both test and comparator datasets, then merging reads from each and estimating the footprinting score of merged reads against the randomized comparator dataset as a percentile. Heatmaps images were obtained via *Java TreeView*. For heatmaps showing the presence of footprinted motifs, sorted by AML/PBSC

footprint probability fold change, motif discovery results were converted to *BED* files and subsequently intersected with digital footprinting results using the *bedtools intersect* function. Footprinted motifs were mapped back to the AML/ PBSC DHS unions by calculating the distance of each footprinted motif to the merged DHS summit *BED* entry, whereby infinity was used if a DHS did not intersect with any footprinted motif. Resulting outputs were converted as distances to summit, and subsequently expressed as tables 200 bp upstream and downstream of each summit using custom Perl scripts, whereby motif frequencies were computed every 10 bp for all regions, ordered according to fold changes. Heatmaps were generated via *Java Treeview*. Motif densities were computed relative to each summit, where distances used were that between the start of each motif (regardless of the strand) and the summit.

Accession numbers

The DNA sequence files associated with this study have been deposited as a superseries in the Gene Expression Omnibus data base (accession number GSE64874). This superseries encompasses individually accessible DNase-Seq datasets GSE64864), ChIP-Seq datasets (GSE64862) and microarray expression datasets (GSE64873)

Public datasets

The previously published Runx1 ChIP-Seq dataset in CD34+ PBSC (Ptasinska et al., 2014) was retrieved from the Gene Expression Omnibus (GEO), accession GSM1466000. Following SRA to FASTQ conversion via the SRA toolkit (version 2.4.7), this sample was processed as other high throughput sequencing samples. ENCODE DNase I chromatin accessibility datasets for CD34+ stem cells, mobilized CD34+ PBSCs and CD14+ cells were retrieved from GEO accessions GSM595919, GSM530652 and GSM701541, respectively (Bernstein et al., 2010; Neph et al., 2012). These samples were processed similarly as above.

Expression profiles in larger patient cohort datasets

Gene expression results from large patient cohort datasets (Cancer Genome Atlas Research Network, 2013; Verhaak et al., 2009) were downloaded from the Leukemia Gene Atlas (Hebestreit et al., 2012) as text files. For data from Verhaak et al., patients were split according to their FLT3-ITD mutational status; for data from the Cancer Genome Atlas Research Network, since only the presence of mutations in the FLT3 gene was screened, patients were split according to their FLT3 mutational status. Probeset expression data was aggregated into per gene average expression data in the case of genes spanning more than one probe. Expression values for 134 and 77 FLT3-ITD up- and down- regulated genes identified in this study were subsequently retrieved using the *merge* function in *R*. Boxplots for individual genes and gene averages were plotted using *R*.

c-Fos ChIP-Seq analysis with and without knock-down in MV4-11 cells

c-Fos ChIP-Seq with mismatch and FLT3 siRNA datasets were processed as described above. To identify whether c-Fos signal changed genome-wide following knock-down, peak summits using the control mismatch siRNA c-Fos ChIP were isolated and average binding profiles were retrieved ±500bp around the summit via the *annotatePeaks* function of *Homer*, using -hist 10 -wig as parameters. Values were smoothed using a moving average of 5 bins (50bp). Average profiles were plotted using *LibreOffice Calc*.

SUPPLEMENTAL REFERENCES

Bernstein, B.E., Stamatoyannopoulos, J.A., Costello, J.F., Ren, B., Milosavljevic, A., Meissner, A., Kellis, M., Marra, M.A., Beaudet, A.L., Ecker, J.R*., et al.* (2010). The NIH Roadmap Epigenomics Mapping Consortium. Nat Biotechnol *28*, 1045-1048.

Bert, A.G., Johnson, B.V., Baxter, E.W., and Cockerill, P.N. (2007). A modular enhancer is differentially regulated by GATA and NFAT elements that direct different tissue-specific patterns of nucleosome positioning and inducible chromatin remodeling. Mol Cell Biol *27*, 2870-2885.

Cancer Genome Atlas Research Network (2013). Genomic and epigenomic landscapes of adult de novo acute myeloid leukemia. N Engl J Med *368*, 2059-2074.

Cockerill, P.N., Shannon, M.F., Bert, A.G., Ryan, G.R., and Vadas, M.A. (1993). The granulocyte-macrophage colony-stimulating factor/interleukin 3 locus is regulated by an inducible cyclosporin A-sensitive enhancer. Proc Natl Acad Sci U S A *90*, 2466-2470.

Dale, R.K., Pedersen, B.S., and Quinlan, A.R. (2011). Pybedtools: a flexible Python library for manipulating genomic datasets and annotations. Bioinformatics *27*, 3423-3424.

de Hoon, M.J., Imoto, S., Nolan, J., and Miyano, S. (2004). Open source clustering software. Bioinformatics *20*, 1453-1454.

DePristo, M.A., Banks, E., Poplin, R., Garimella, K.V., Maguire, J.R., Hartl, C., Philippakis, A.A., del Angel, G., Rivas, M.A., Hanna, M*., et al.* (2011). A framework for variation discovery and genotyping using next-generation DNA sequencing data. Nat Genet *43*, 491-498.

ENCODE Project Consortium (2012). An integrated encyclopedia of DNA elements in the human genome. Nature *489*, 57-74.

Fenouil, R., Cauchy, P., Koch, F., Descostes, N., Cabeza, J.Z., Innocenti, C., Ferrier, P., Spicuglia, S., Gut, M., Gut, I*., et al.* (2012). CpG islands and GC content dictate nucleosome depletion in a transcription-independent manner at mammalian promoters. Genome Res *22*, 2399-2408.

Hebestreit, K., Grottrup, S., Emden, D., Veerkamp, J., Ruckert, C., Klein, H.U., Muller-Tidow, C., and Dugas, M. (2012). Leukemia gene atlas--a public platform for integrative exploration of genome-wide molecular data. PLoS One *7*, e39148.

Heinz, S., Benner, C., Spann, N., Bertolino, E., Lin, Y.C., Laslo, P., Cheng, J.X., Murre, C., Singh, H., and Glass, C.K. (2010). Simple combinations of lineage-determining transcription factors prime cis-regulatory elements required for macrophage and B cell identities. Molecular cell *38*, 576-589.

Kelly, L.M., Liu, Q., Kutok, J.L., Williams, I.R., Boulton, C.L., and Gilliland, D.G. (2002). FLT3 internal tandem duplication mutations associated with human acute myeloid leukemias induce myeloproliferative disease in a murine bone marrow transplant model. Blood *99*, 310-318.

Koch, F., Fenouil, R., Gut, M., Cauchy, P., Albert, T.K., Zacarias-Cabeza, J., Spicuglia, S., de la Chapelle, A.L., Heidemann, M., Hintermair, C*., et al.* (2011). Transcription initiation platforms and GTF recruitment at tissue-specific enhancers and promoters. Nat Struct Mol Biol *18*, 956-963.

Kreher, S., Bouhlel, M.A., Cauchy, P., Lamprecht, B., Li, S., Grau, M., Hummel, F., Kochert, K., Anagnostopoulos, I., Johrens, K*., et al.* (2014). Mapping of transcription factor motifs in active

chromatin identifies IRF5 as key regulator in classical Hodgkin lymphoma. Proc Natl Acad Sci U S A *111*, E4513-4522.
Li, H., Handsaker, B., Wysoker, A., Fennell, T., Ruan, J., Homer, N., Marth, G., Abecasis, G., and Durbin, R. (2009). The Sequence Alignment/Map format and SAMtools. Bioinformatics *25*, 2078-2079.
Neph, S., Vierstra, J., Stergachis, A.B., Reynolds, A.P., Haugen, E., Vernot, B., Thurman, R.E., John, S., Sandstrom, R., Johnson, A.K.*, et al.* (2012). An expansive human regulatory lexicon encoded in transcription factor footprints. Nature *489*, 83-90.
Piper, J., Elze, M.C., Cauchy, P., Cockerill, P.N., Bonifer, C., and Ott, S. (2013). Wellington: a novel method for the accurate identification of digital genomic footprints from DNase-seq data. Nucleic Acids Res *41*, e201.
Ptasinska, A., Assi, S.A., Mannari, D., James, S.R., Williamson, D., Dunne, J., Hoogenkamp, M., Wu, M., Care, M., McNeill, H.*, et al.* (2012). Depletion of RUNX1/ETO in t(8;21) AML cells leads to genome-wide changes in chromatin structure and transcription factor binding. Leukemia *26*, 1829-1841.
Ptasinska, A., Assi, S.A., Martinez-Soria, N., Imperato, M.R., Piper, J., Cauchy, P., Pickin, A., James, S.R., Hoogenkamp, M., Williamson, D.*, et al.* (2014). Identification of a Dynamic Core Transcriptional Network in t(8;21) AML that Regulates Differentiation Block and Self-Renewal. Cell Reports *8*, 1974-1988.
Quinlan, A.R., and Hall, I.M. (2010). BEDTools: a flexible suite of utilities for comparing genomic features. Bioinformatics *26*, 841-842.
Saldanha, A.J. (2004). Java Treeview--extensible visualization of microarray data. Bioinformatics *20*, 3246-3248.
Smyth, G.K., Michaud, J., and Scott, H.S. (2005). Use of within-array replicate spots for assessing differential expression in microarray experiments. Bioinformatics *21*, 2067-2075.
Tam, W.F., Gu, T.L., Chen, J., Lee, B.H., Bullinger, L., Frohling, S., Wang, A., Monti, S., Golub, T.R., and Gilliland, D.G. (2008). Id1 is a common downstream target of oncogenic tyrosine kinases in leukemic cells. Blood *112*, 1981-1992.
Verhaak, R.G., Wouters, B.J., Erpelinck, C.A., Abbas, S., Beverloo, H.B., Lugthart, S., Lowenberg, B., Delwel, R., and Valk, P.J. (2009). Prediction of molecular subtypes in acute myeloid leukemia based on gene expression profiling. Haematologica *94*, 131-134.
Ye, K., Schulz, M.H., Long, Q., Apweiler, R., and Ning, Z. (2009). Pindel: a pattern growth approach to detect break points of large deletions and medium sized insertions from paired-end short reads. Bioinformatics *25*, 2865-2871.
Zhu, L.J., Gazin, C., Lawson, N.D., Pages, H., Lin, S.M., Lapointe, D.S., and Green, M.R. (2010). ChIPpeakAnno: a Bioconductor package to annotate ChIP-seq and ChIP-chip data. BMC Bioinformatics *11*, 237.